The Evolution of Surface Symmetry in Femtosecond Laser-Induced Transient States of Matter

By

Joy Carleen Garnett

Dissertation

Submitted to the Faculty of the

Graduate School of Vanderbilt University

in partial fulfillment of the requirements

for the degree of

DOCTOR OF PHILOSOPHY

in

Interdisciplinary Materials Science

May, 2017

Nashville, Tennessee

Approved:

Norman H. Tolk, Ph.D.

Jim Davidson, Ph.D.

David J. Ernst, Ph.D.

Kalman Varga, Ph.D.

Timothy P. Hanusa, Ph.D.

ACKNOWLEDGEMENTS

I would like to express the deepest appreciation to my committee chair, Professor Norman Tolk. He continually conveyed a spirit of skeptical exploration about research. Without his guidance, this dissertation would not have been possible. To my committee, I am extremely grateful for your assistance and suggestions throughout my project.

I would also like to thank past and present Tolk group members, especially Dr. Halina Krzyzanowska, Dr. Stephanie Gilbert-Corder, Dr. Jennifer Jones, and Andrey Baydin, for their training and support. I am grateful to them for showing confidence in my work, as well as for their patience and help. A special word of gratitude is due to Marilyn Holt and Andrey Baydin, who has read and commented on several chapters.

I am also indebted to the staff of the PCC for their support and cooperation.

I thank the staff of the Vanderbilt Institute of Nanoscale Science and Engineering, who assisted with this and previous projects. I would also like to thank the staff from the Department of Physics and Astronomy at Vanderbilt University for their support. Financial support was provided by Vanderbilt University, the Fisk-Vanderbilt Bridge Program, DOE Basic Energy Sciences Grant #DE-FGO2-99ER45781, ARO Contract Number #W911NF-14-1-0290, and a GEM Full Fellowship from the National GEM Consortium.

Finally, I would like to acknowledge with gratitude, the support and love of my family and previous teachers– my mother, Ms. Carleen Garnett; my childhood friends, Vanessa Espinoza Katz, Megan Wimberley, Jennifier Henderson Brown and their families; Mr. Howard Denton, Ms. Renee Rogers, and Ms. Kathleen Griffin; and Mr. Michael Hehnen. Without them, this dissertation would not have been possible.

TABLE OF CONTENTS

LIST OF TABLES

LIST OF FIGURES

Chapter 1

Introduction

Gallium arsenide and other III-V materials are well known for their excellent optical and electronic properties and have led to the development of high-performance photovoltaic cells[1,2], photoelectrochemical water splitting[3,4], and light emitting diodes (LEDs)[5]. Several combinations of III-V semiconductors are now being considered as potentially attractive alternatives to silicon for these applications. However, further development requires fundamental understanding of processes that govern light-matter interactions. Specifically, surface strain and ultrafast dynamics are of great interest to the optoelectronic industry.

Strained semiconductor surfaces dominate the design of optoelectronics and III-V semiconductor-based LEDs. Currently, the structures of strained surfaces are well characterized with x-ray diffraction (XRD)[6] and electron crystallography[7-9]. However, optically-induced electronic behavior at these interfaces are not fully understood. This has the been one of the stimulants for the research in this dissertation. To further explore optically-induced electronic behavior at strained interfaces, I have asked the following questions:

1. How does static optoelectronic behavior change as a function of strain?
2. How does surface symmetry and electronic motion change with respect to strain?
3. How do atomic bonds change as a function of strain?

Another main research goal of this work is to understand ultrafast subpicosecond processes after pulsed laser excitation. The knowledge of ultrafast processes dominates the design of devices in industries that require high temporal and spectral resolution. Ultrafast atomic motion has been the major focus of subpicosecond structural dynamics. Currently, these dynamics upon photoexcitation are well characterized with experimental methods such as ultrafast x-ray diffraction (U-XRD), ultrafast electron diffraction (UED), and ultrafast electron crystallography (UEC). However, ultrafast atomic motion does not occur alone. The bonds connecting these moving atoms are also affected during this process. The correlation between structural and electronic dynamics is not well understood.

To further explore correlated structural and electronic behavior upon ultrafast laser excitation, I have asked the following questions:

1. How does subpicosecond optoelectronic behavior change as a function of time after femtosecond pulse photoexcitation?
2. How does subpicosecond surface symmetry and electronic motion change with respect to time after femtosecond pulse photoexcitation?
3. How do atomic bonds change as a function of time after femtosecond pulse photoexcitation?

To address these questions, I used experimental methods sensitive to both atomic motions and electronic responses: polarization-resolved second harmonic generation (PRSHG) and time-resolved, polarization-resolved second harmonic generation (TR-PRSHG). The dissertation covers application of these techniques to III-V semiconductors: gallium arsenide (GaAs), gallium antimonide (GaSb), and aluminum gallium arsenide (AlGaAs).

This dissertation is organized as follows. Chapter 2 presents the background of electronic band structures, ultrafast relaxation processes, and the origin of nonlinear optics from the perspectives of classical and quantum mechanics. It thus provides a framework for the static and transient nonlinear optical processes observed in III-V semiconductors under ultrafast pulse excitation.

Next, Chapter 3 motivates the use of the experimental and analytical methods as applied to the experimental and theoretical studies outlined in Chapters 4 and 5. Chapter 4 is devoted to the understanding of polarization-resolved second-order nonlinear optical responses of various strained III-V semiconductor heterostructures resulting from defect-conducive growth conditions. Simplified phenomenological expressions for the polarization-resolved second harmonic generation (PRSHG) are first derived using tensor analysis. Afterwards, these expressions are used to fit experimental data. The developed formalism is tested under different conditions to gauge the fit robustness and sensitivity to mechanical and electronic changes in strained III-V semiconductors.

Along that same vein, Chapter 5 extends this analytical fit to describe ultrafast PRSHG responses of GaAs (100) as a function of transient changes in the interatomic potential within the first picosecond after photoexcitation. Finally, the dissertation concludes with Chapter 6 addressing possible directions for future

work. The chapter begins with a description of studies to further test the sensitivity and robustness of the PRSHG phenomenological fit and how it can be used to characterize more classes of materials.

Chapter 2

Background

In this dissertation, my goal was to further understand correlated structural and electronic behaviors upon ultrafast laser excitation. In this chapter, I provide a framework for describing static and transient nonlinear optical responses observed in III-V semiconductors by presenting a background of electronic band structures, ultrafast relaxation processes, and the origin of nonlinear optics from the perspectives of classical and quantum mechanics. These topics are related in that they involve linear and nonlinear subpicosecond optical responses in III-V semiconductors excited undergoing excitation above the band gap. The characteristics of nonlinear optics described briefly in the following section provide an introduction to the theory behind the experimental methods and analyses used in the research in this dissertation.

2.1. Nonlinear Optics Overview

What is nonlinear optical behavior?

In materials, the incident optical field has a profound effect on the resultant linear or nonlinear optical response. The linear optical response is linearly proportional to the incident electric field, whereas, the nonlinear optical response is not. The nonlinear response can have quadratic, cubic, or higher order dependencies on the incident optical electric field. Thus, the term 'nonlinear' involves a wide variety of optical responses.

Factors influencing nonlinearities are directly related to the nature of an anharmonic interatomic potential or dipole moment and subsequently induced polarization in a combination of optical fields. Such factors can be described mathematically. First, let us consider a material with a dipole moment per volume (?) that undergoes an induced linear polarization:

$$P(t) = \epsilon_o \chi^{(1)} E(t) \quad (1)$$

where ϵ_o is the permittivity of free space ($8.85418782 \times 10^{-12}$ m^{-3} kg^{-1} s^4 A^2) and $\chi^{(1)}$ is the linear optical susceptibility (dimensionless).

However, in the case of nonlinearity, the induced polarization is not linearly proportional to the incident electric

field. As stated above, it can have a quadratic, cubic, or higher order proportionality. Mathematically, this dependence on the incident electric field can be expanded as a power series

$$P(t) = \epsilon_o \chi^{(1)} E(t) + \epsilon_o \chi^{(2)} E^2(t) + \epsilon_o \chi^{(3)} E^{3(t)} + \cdots \quad (2)$$

where $\chi^{(2)}$ and $\chi^{(3)}$are the second- and third-order nonlinear optical susceptibilities (m/V and m^2/V^2), respectively.

Such nonlinear responses can be classified by order. For instance, induced polarizations with a quadratic dependence on the incident electric field are known as second order and those with cubic dependence are known as third order. In this dissertation, I focus on second order nonlinearities since they are sensitive to crystalline order and thus have been used as reliable optical characterization methods of the crystal symmetries of solids.

Second order nonlinear optical processes can be further organized by the input and output optical electric field frequencies as mathematically shown below:

- Second harmonic generation (SHG).
  - $P(2\omega_1) = \epsilon_o \chi^{(2)} E_1^2$
- Sum frequency generation (SFG).
  - $P(\omega_1 + \omega_2) = 2\epsilon_o \chi^{(2)} E_1 E_2$
- Difference frequency generation (DFG).
  - $P(\omega_1 - \omega_2) = 2\epsilon_o \chi^{(2)} E_1 E_2$
- Optical rectification(OR).
  - $P(0) = 2\epsilon_o \chi^{(2)} (E_1 E_1 + E_2 E_2)$

Either of these processes can be used to characterize the crystal symmetry in solids. The most straightforward method is to second harmonic generation (SHG), since it is the only one that can be performed with a single input frequency. The other three require two input frequencies. Therefore, the SHG was chosen as a main tool to study material properties under consideration in this dissertation because of its ease of implementation.

The remainder of this chapter covers background topics relevant to SHG. First, I review the current understanding of the macroscopic physical origin of SHG. Particularly, the physical origin can be understood microscopically as either bond charge movement or macroscopically as centrosymmetry. To approximate the

nonlinear response to macroscopic quantities, formalisms are incredibly helpful. There are two major formalisms that can describe 2nd order nonlinear behavior: classical and quantum mechanical. Finally, I review the classical and quantum mechanical formalisms of second order nonlinear behavior, paying special attention to $\chi_{ijk}^{(2)}$.

Second Harmonic Generation

Second order nonlinear optics (2nd order NLO) covers diverse topics. Studies of second order optical nonlinearities are necessary for the characterization of noncentrosymmetric crystals. Depending on experimental conditions, characterization methods can involve one or more types of 2nd order NLO described in the previous section. Of the above types, we turn our attention to second harmonic generation (SHG). It is also referred to as frequency doubling of an input fundamental frequency ω_1 to the second harmonic $2\omega_1$ (or ω_2). In this section, I review classical and quantum descriptions of second order nonlinear optics.

As can be understood from the name, second harmonic generation occurs when the power at incident frequency (ω) converts to power at frequency at the second harmonic frequency (2ω). As shown in Figure 2.1, two photons of frequency omega are converted into a single photon of frequency 2ω through a quantum-mechanical process involving a virtual level (dashed line) and ground state (solid line). However, this isn't the only contribution to the reflected beam. It is a combination of three contributions: a zero frequency (a constant), incident frequency (ω), and the second harmonic frequency (2ω) contributions as shown below.

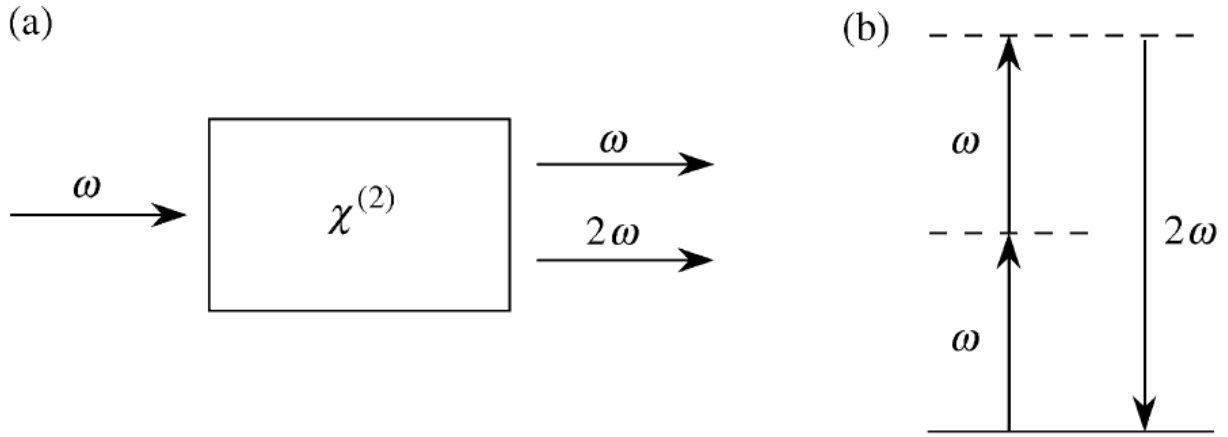

Figure 2.1: (a) Geometry of second harmonic generation. (b) Energy-level diagram describing second harmonic generation[13].

From around the late 1960s, there was a growing awareness that nonlinear optical (NLO) properties can be modeled in a more practical way than quantum mechanical statistics. This led to the birth of a much simpler approach of understanding NLO properties. This approach is called the bond-charge model. It considers NLO properties as a natural consequence of the localized movement of an atom's bound outer valence electrons. The bond charge model developed by Levine[10,11] relates linear and higher-order polarizabilities to bonds interacting with applied electric fields. Simply put, NLO properties of a material can be described by the unequal movement of an electron between two dissimilar elements with the bond-charge model.

The first stage in this model is the definition of a bond connecting A and B atoms of different elements. The bond is defined as a single point charge *q* between A and B with a bond length *d* described as the addition of the covalent radii r_A and r_B, respectively. This configuration in shown in Figure 2.2. The NLO behavior is the calculation of the movement of point charge *q* between atoms A and B with expected coupling of an applied electric field *E* in a given bond polarization.

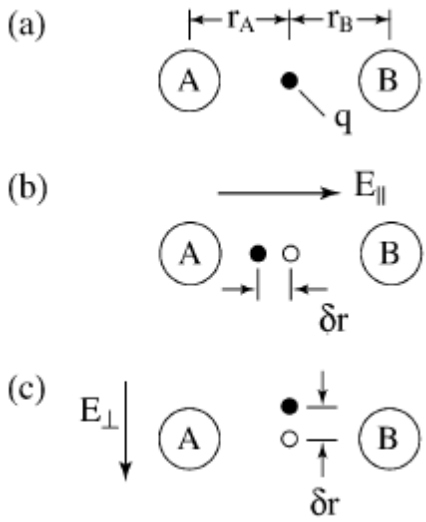

Figure 2.2: The bond-charge model applied to a chemical bond between elements A and B. Parts (b) and (c) show how the charge moves in response to applied electric fields. Source: Boyd[13]

Classical formulation of $\chi_{ijk}^{(2)}$: Nonlinear susceptibility as a classical anharmonic oscillator

Modeling optical responses as oscillators works for visualizing electronic motion in an optical field. In this

oscillator model, the electronic motion is dominated by the restoring force exerted on the electron undergoing this field. The idea that the nonlinear optical response can be modeled as a harmonic or anharmonic oscillator is an accurately simple one. In fact, the electron-nucleus interaction can be accurately compared to a spring. It is generally agreed that the spring mirrors Coulomb forces dominating the interplay between binding electron attraction and repulsion from the nearest neighbor nuclei. Conceptually, the case of an oscillator driven by an outside force is similar to the case of a bound electron driven by an applied electric field. Another term for this interplay of forces is the interatomic potential. Any nonlinearities developed during this external driving of the interatomic potential are due to uneven stretching and/or compression of this "spring". In terms of electronic motion, this means that unequal motion along the bond caused by uneven Coulomb forces or uneven interatomic potentials produce a nonlinear optical response.

As stated above, two related but different oscillators are associated with nonlinear optics, namely the driven harmonic oscillator and the driven anharmonic oscillator. The harmonic oscillator model applies when the Coulomb forces imparted on the electron residing between bonded atoms are equal. Thus, the interatomic potential is considered even and harmonic. Materials with harmonic potentials are referred to as centrosymmetric. Usually, centrosymmetric semiconductors are composed of a single chemical element, such as germanium or silicon. Another thing to consider is that due to this even interatomic potential, second-order nonlinearities are not observed but third-, fifth-, seventh- and higher odd-order ones are.

In 2nd order NLO, nonlinearity can be approximately simulated using a classical anharmonic oscillator. In fact, the approach of a particle moving in a classical anharmonic oscillator is adequate for describing uneven electronic motion in a noncentrosymmetric material. This inequality can be quantified as a measure of anharmonicity. Materials exhibiting this anharmonicity are conventionally referred to as noncentrosymmetric. Consider a material with an anharmonic potential shown in Figure 2.3. This interatomic potential energy, energy density, and motion produces nonlinear polarization that couples to the incoming optical field and produces second-order electromagnetic radiation. Although the conclusions of this model do not yield quantitative parameters, the qualitative understanding is physically and intuitively sound.

As described above, second order nonlinear optical behavior is absent in centrosymmetric materials. As centrosymmetry has such

a significant influence on second order nonlinear behavior, it indirectly relates to the symmetry of second order nonlinear optical susceptibility ($\chi_{ijk}^{(2)}$) tensor described in Equation 2. This uneven electronic motion produces a net lattice polarization, which profoundly influences the optical response. Factors influencing this lattice polarization are the type and nature of electronic motion.

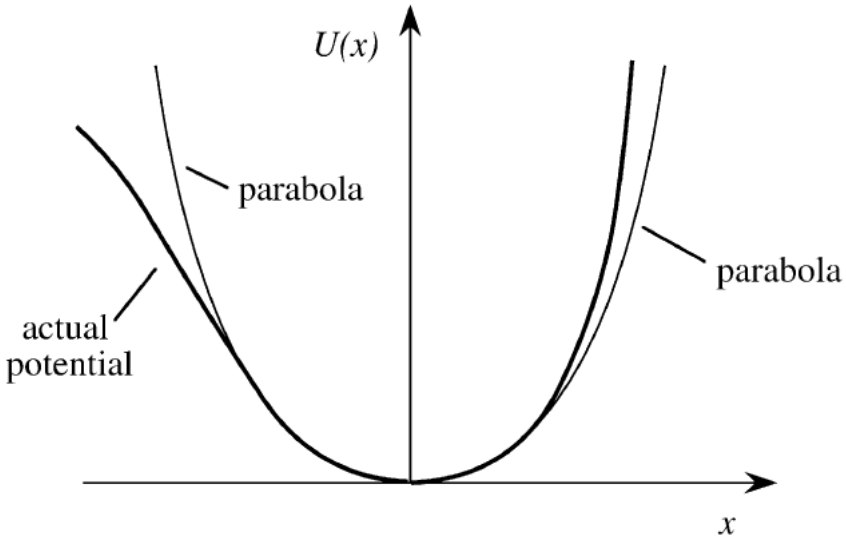

Figure 2.3: Anharmonic potential energy function for a noncentrosymmetric medium. Source: Boyd[12]

Quantum Mechanical Formalism of $\chi_{ijk}^{(2)}$: Nonlinear optical susceptibility as dipole transition populations

Second order NLO can also be described with a quantum mechanical formalism. Specifically, it can be described as the product of an electronic transition process undergoing a three-photon exchange involving real and virtual levels. To obtain an appropriate description of 2nd order NLO with dipole populations between real and virtual levels, suitable context is necessary. The idea that 2nd order NLO can be described as electronic transitions between levels is a considerable idealization. This section reviews the description of second order nonlinear optical properties as an electronic transition. The ways of estimating electronic dipole contributions to nonlinear behaviors are outlined.

As mentioned in Section 2.1, 2nd order NLO in a material depends on the second order nonlinear optical susceptibility tensor ($\chi_{ijk}^{(2)}$). The subscript ijk refers to Cartesian directions x, y, and z and the superscript (2) denotes second order nonlinearity

for electric fields and induced polarization. It can be thought of as a measure of the nonlinearity in all directions resulting primarily from anharmonicity of the electronic motion in the presence of an optical field. This susceptibility is conveniently expressed as dipole populations along the *j* and *k* directions producing a resultant 2nd order NLO response in the *i* direction. Such optical behavior is evaluated through studies of two main components: real levels and virtual levels. As shown in Figure 2.1, two photons of frequency ω are converted into a single photon of frequency 2ω through a quantum-mechanical process involving a virtual level (dashed line) and a real level ground state (solid line). These two components are complementary, and for the best understanding should be described together.

Explicit descriptions of dipole population behavior during SHG involves the consideration of three major factors: atomic energy levels, internal symmetries of the susceptibility, and the dipole transition moments. These three factors are required for the preparation of a functional form of the dipole moment populations as they relate to specific nonlinear susceptibility tensor elements. It can involve one or more of the following topics:

- Existence and contribution of real and virtual levels to nonlinear optical behavior,
- Resonant dipole transitions between real and virtual levels, and
- Relaxation processes between real and virtual energy levels contributing to transient nonlinear optical behavior.

Since the focus of this dissertation is SHG, the following description of dipole populations along *j* and *k* is considered along equally spaced real and virtual levels n, m, and g shown in Figure 2.4. For a given material, the second order susceptibility tensor can be expressed as dipole transitions between excited states n, m, and g, by the following equation

$$\chi_{ijk}^{(2)}(\omega_\sigma, \omega_q, \omega_p) = \frac{N}{\epsilon_o \hbar^2} P_F \sum_{mn} \frac{\mu_{gn}^i \mu_{nm}^j \mu_{mg}^k}{(\omega_{ng} - \omega_\sigma)(\omega_{mg} - \omega_p)}, \quad (3)$$

where N is the number of dipoles undergoing the transition, ϵ_o is the permittivity of free space, P_F is the permutation operator summed over all permutations of input frequencies ω_p and ω_q and

output frequency ω_o, μ_{gn}^{i} is the electric dipole transition moment in the *i* direction between levels g and n, μ_{nm}^{j} is the electric dipole transition moment in the *j* direction between levels m and n, μ_{mg}^{k} is the electric dipole transition moment in the *k* direction between levels g and m, ω_{ng} is the transition frequency between levels n and g, and ω_{mg} is the transition frequency between levels m and g. The term ω_{ng} is defined as $\omega_{ng} = \frac{E_n - E_g}{\hbar} - \frac{i\Gamma_n}{2}$ where Γ_n is the population decay rate of level n. Along the same line, the term ω_{mg} is defined as $\omega_{mg} = \frac{E_m - E_g}{\hbar} - \frac{i\Gamma_m}{2}$ where Γ_m is the population decay rate of level m.

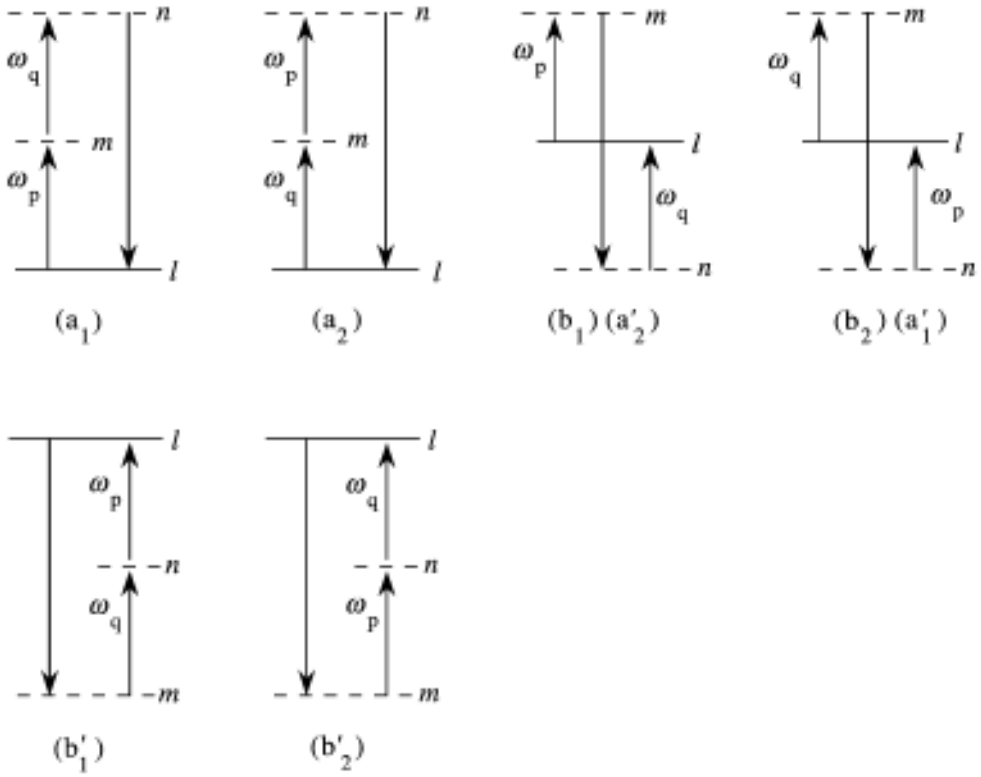

Figure 2.4: The quantum resonances in the second order susceptibility $\chi_{ijk}^{(2)}$ Source: Boyd[13]

Thus, the value of the second order nonlinear susceptibility tensor is linearly related to the sum of the excited dipole transition populations within a given volume. This way of calculating $\chi_{ijk}^{(2)}$ is better at estimating the rate of transition for materials with sharp atomic levels like atomic vapors and molecular compounds and not broadened levels as with solids. However, it does give a qualitative comparison of the relative $\chi_{ijk}^{(2)}$ tensor elements with respect to each other in terms of dipole populations along the i, j, and k directions.

In Figure 2.4, it is seen that there are three possible mechanisms for generating second order nonlinear optics. All three mechanisms are considered in the calculation of the second order nonlinear optical susceptibility ($\chi_{ijk}^{(2)}$) tensor elements. To estimate the dominant mechanism, the degree of contribution between these three mechanisms are described by the relationships between the real and virtual levels and the incoming and outgoing frequencies. In semiconductors that have a band gap, the dominant mechanism depends heavily on the incident light frequency and resonant frequencies (local conduction band minima) of the material.

For SHG analyses in Chapters 4 and 5, the responses are described in terms of the second order nonlinear optical susceptibility tensor elements and their relevant dipole populations along *j* and *k* directions. These are adequate for describing the structural responses of III-V semiconductors under various conditions. In fact, this analysis is warranted for detailed investigation of transient dipolar behaviors as well.

2.2. Electronic Band Structures of Semiconductors

In semiconductors, discussion of electronic behavior should obviously include a review about the periodic nature of the lattice and its environment that will allow adequate evaluation of the electronic band structure. The scope of this review includes the description of band theory. To obtain the maximum benefit from any analytical method of ultrafast or static nonlinear optical response, an understanding of the physical origins of the band structure is essential and are reviewed here. An overview of the characteristics of electronic band structures provide an introduction to photoexcitation dynamics, which are described in the Section 2.3.

What is a semiconductor?

Semiconductors comprise many electronic and optoelectronic devices useful to the computer and solar cell industries. In semiconductors, the electronic band structure has a profound influence on the optical response. Factors influencing the optical response are the geometry of the band structures and laser wavelength. Thus, the study of laser-induced behaviors in semiconductors involve excited electronic generation and decay populations as well as their associated optical responses. For most purposes, it is necessary to have quantitative measures for defining semiconductors. This is conveniently done in terms of carrier density *n*, conductivity σ, and energy gap E_g. The gap is

defined as the energy difference between occupied and empty states. In semiconductors, the conduction band (CB) and valence band (VB) should ideally be analyzed as an electronic continuum. Although in practice, each part of the band structure should be considered as part of the whole when considering light-matter interactions. The characteristics of band structures are numerous and some of the more important ones are reviewed below.

The electronic band structures of semiconductors can be classified into two categories: direct and indirect band gap. Indirect band gap materials have their conduction band minimum (conduction band edge) and the valence band maximum (valence band edge) at the different points in the Brillouin zone. Appropriate examples of an indirect band gap material would be Group IV semiconductors, such as silicon or germanium. Direct band gap materials have their conduction band minimum (conduction band edge) and the valence band maximum (valence band edge) at the same point in the Brillouin zone. Relevant examples of a direct band gap material would be group III-V semiconductors, such as gallium arsenide (GaAs) and gallium antimonide (GaSb). Figure 2.5 displays examples of an indirect band gap material (silicon) and a direct band gap material (GaAs) for comparison. For the rest of this section, I limit the discussion to III-V semiconductors, as it is relevant to the studies in this dissertation.

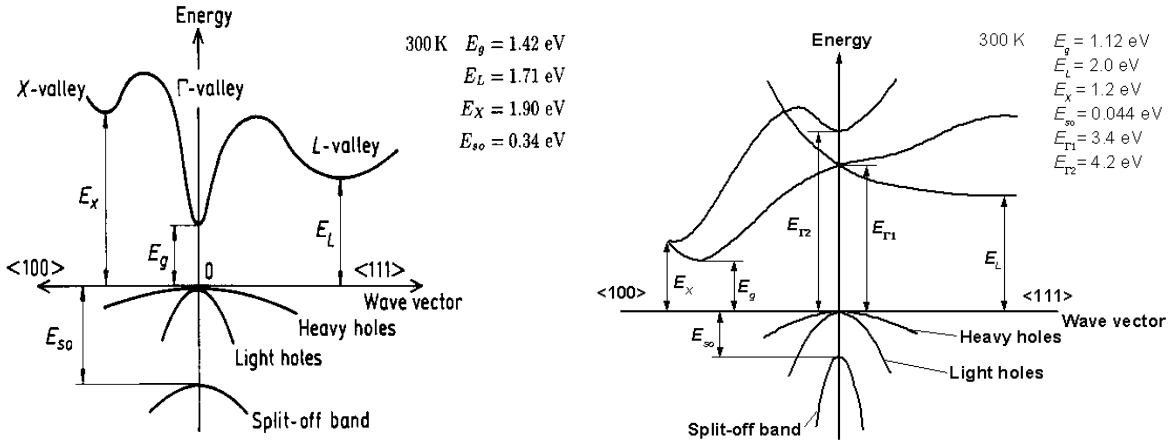

Figure 2.5: The band structures of (a) direct-band gap GaAs and(b)indirect-band gap Si. Source: Ioffe Institute.

Energy gap characteristics are directly connected to the type of atomic bonding. In covalently bonded materials where the electrons are shared between atoms, such as silicon or gallium arsenide, the energy gaps are small and wide enough to produce a moderate carrier density ($< 10^{17}$ cm^{-3}) and conductivity (10^{-9} cm^{-1} – 10^{2} cm^{-1}). In materials where the bonds are highly ionic,

manifestations of small band gaps characteristics do not occur. Instead, these situations produce fairly low carrier densities (<< 1 cm^{-3}) and conductivities (< 10^{-9} cm^{-1}), where not many electrons transition between the valence and conduction bands. However, some insulators that become semiconductors at high temperature, or wide band gap materials, have been of great interest as of late.

Optical absorption and emission in semiconductors

In semiconductors, laser wavelength has a profound effect on carrier generation and scattering, thermal equilibration, recombination, and thermal diffusion rates. At energies far below the band gap, light is not absorbed and no electron-hole pairs are created. However, at laser wavelengths above the band gap ($h\nu > E_g$), optical absorption transitions in semiconductors can be either direct or indirect, depending on their band structures.

To quantify the influence of absorption on semiconductors for optoelectronic applications, it is necessary to identify the patterns in electronic band structures, energetic transitions, and radiative lifetimes. Understanding the forces involved in absorption and identifying the electronic band features in a semiconductor enable the formulation of relationships between incident electromagnetic radiation and resultant optical responses. These relationships involve the careful mapping of electron-radiation interactions within an electronic band, and the correlation of these interactions with models of optical transitions. Aspects of this are further discussed in Section 2.3.

2.3. Relaxation Processes of Photoexcited Semiconductors

Femtosecond lasers have proven to be useful in illuminating scattering dynamics of nonequilibrium photoexcited carriers in semiconductors. The interest in these carrier dynamics arises mainly from the needs of the microelectronic and photonic industries. Dynamics of band structure, scattering events, carrier diffusion, and other effects are vital in understanding semiconductor transport theory and carrier dynamics. A working knowledge of these topics is essential for optimal designs of future optoelectronic devices. Semiconductor physics tells us about the electronic and optical response upon photoexcitation, which may differ greatly depending on incident wavelength and pulse width. While the concepts of this section apply to all semiconductors regardless of band structure, any discussion of photoexcitation is generally confined to events seen in direct band gap materials. While semiconductor transport applies to all excitations regardless of generation method, any discussion of

excitations in this work is generally confined to events derived from femtosecond photoexcitation.

The goal of this section is not to review all transport topics, but instead to provide an introductory overview of carrier and phonon dynamics of moderately excited ($< 10^{18}$ cm^{-3}) semiconductors. In this regard, I will focus on the case of polar semiconductors, specifically GaAs. In the following discussion, emphasis is placed more on processes that can be directly observed with ~50 fs laser resolution than on exhaustive descriptions for all interactions. As has been stressed in Chapter 1, there is a great need for understanding how carrier interactions before thermal equilibrium correlate to subpicosecond optical responses in the subject of scattering in semiconductor dynamics.

Scattering arises mainly from interactions between the lattice and excited electrons and holes. In some materials, these events occur on the subpicosecond timescale, making femtosecond measurements useful for probing the effects these events have on optical properties of the material. These scattering events can be seen to follow clearly defined processes which form a temporal evolution of energy and momentum decay called relaxation.

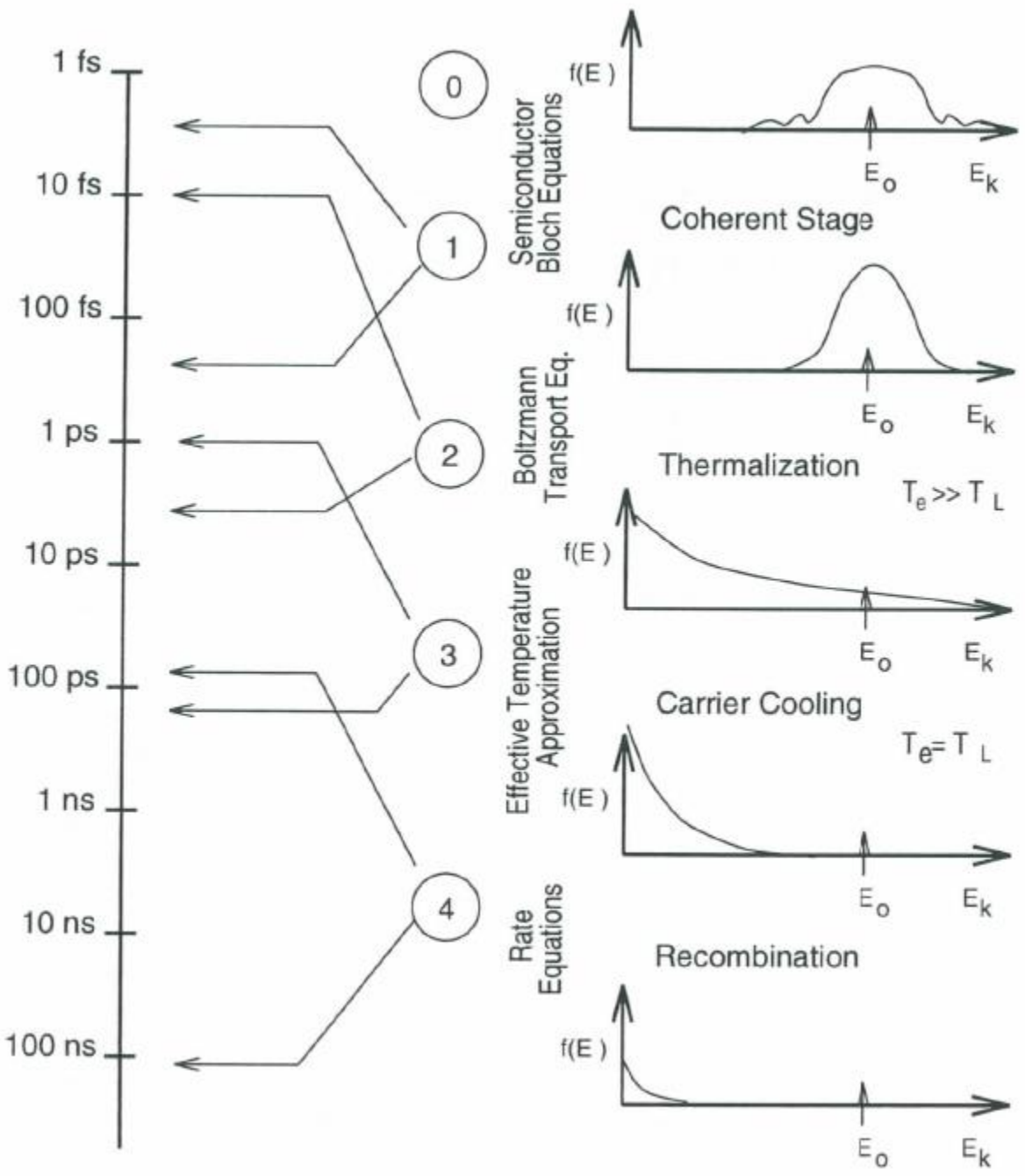

Figure 2.6: Time scale for different stages of relaxation phenomena in photoexcited experiments. Source: Stanton[80]

To analyze ultrafast nonlinear optical spectroscopy, it is essential to review the current understanding of temporal regimes of relaxation processes in polar semiconductors related to nonequilibrium carrier transport after photoexcitation in polar semiconductors. We thus need to review the four ultrafast physical

processes that happen during relaxation of a semiconductor photoexcited with an ultrashort pulse. These regimes are generally classified by changes in both carrier and lattice temperatures, which produce unique optical responses. To fully account for the changes in carrier and lattice temperature, not only the energetic and momentum relaxation processes have to be considered, but also associated excited dynamics such as scattering, decoherence, and recombination.

In the initial stages of relaxation, the photoexcited electron and hole share the same energy and momentum, meaning that they are coherent. This state is described with semiconductor Bloch equations and retains this behavior for about 10 fs. These coherent carriers collide with each other, modifying the energy distribution through a process known as dephasing. Dephasing modifies the carrier distributions from one that can be described with semiconductor Bloch equations to those that are more readily described with either Fermi-Dirac or Maxwell-Boltzmann distribution functions. This change is described through the Boltzmann transport equation. Once the carrier distributions have reached either a Fermi-Dirac or Maxwell-Boltzmann distribution function, this event is known as thermalization, where the electrons can be described as having the same effective temperature.

The progressive decrease in effective electron temperature causes a related increase in effective lattice temperature through a process known as carrier cooling. This transfer of temperature or energy can be described by the effective temperature approximation and signals thermal equilibrium when the lattice and electron temperature are equal. Once the excited carriers and the lattice reach thermal equilibrium, this leads to an accumulation of carriers at the conduction band edge until they are relieved by a longer event called electron-hole recombination. Depending on the semiconductor, recombination can occur from hundreds of picoseconds until hundreds of nanoseconds. Recombination ends when the all electrons have recombined with holes.

To review, ultrafast relaxation behaviors in the following order:

- Coherent regime (< 200 fs),
- Nonthermal regime (< 2 ps),
- Hot carrier regime (1 - 100 ps), and
- Isothermal regime (> 100 ps).

Another step in relating ultrafast transient optical responses to dynamic carrier phenomena is to identify all the contributing factors as discussed below.

Coherent Regime (< 200 fs)

In the above temporal classification, the coherent regime is defined in terms of phase coherence of the carriers with incident optical polarization, also known as the electric field of the incident pulse. This coherence is lost usually within 200 fs after excitation.

Nonthermal regime (< 2 ps)

By the term *nonthermal*, it is generally understood that this is before the carriers reach a common temperature. Processes that happen in the nonthermal regime are of major interest to the optoelectronics and high-speed electronic industries. For these applications, nonthermal processes are studied extensively by those looking to create faster and more energy-efficient device designs. The dominant contributions to the transient optical responses are directly related to the loss of coherence of the excited carriers to the incident electric field / optical polarization discussed earlier. Different materials have different decoherence timescales, sometimes for the same incident energies.

The major outcomes of decoherence are twofold. The first outcome is to allow electrons and holes to reach the same energetic distribution with themselves, which takes a few hundred femtoseconds. The second outcome is to allow the excited electrons and holes to reach the same carrier energetic distribution with each other, which can take up to several picoseconds. This is achieved through carrier-carrier scattering.

Hot carrier regime (1-100 ps)

In this regime, the carriers can be considered to have a common carrier temperature and are no longer considered nonthermal. The dynamics of excited electrons and holes in the hot carrier regime deals with similar relaxation processes in principle as are faced in macroscopic thermal transport. However, the timescale of nanoscopic thermal transport are considerably shorter than macroscopic transport because of the much shorter path lengths involved. These differences are magnified by rapidly changing interconnected electronic processes (especially with higher carrier densities), phonon-influenced changes in the band structure, surface states, and the presence of surface electronic

fields. Carrier cooling, the dominant feature in this regime, happens when the common excited carrier temperature heats the lattice temperature until they reach equilibrium.

There are many processes for excited carriers at a common temperature to release energy to the lattice, which may be divided into two types: electron-phonon scattering and phonon-phonon scattering. These scattering events allow excited carriers to relax into energetically broad thermal distributions. While phonon-related processes are the major contributor to thermal equilibrium between the carriers and the lattice, the timescales vary depending on the material rather than the phonon processes themselves.

Isothermal regime (> 100 ps)

The *isothermal regime* is the name often given to the period after the lattice and carriers reach the same temperature, conventionally known thermal equilibrium. At this stage in the relaxation, the excited carriers then decay through two types of recombination: radiative and nonradiative recombination. Depending on the material and excitation parameters, recombination can range from around 100 picoseconds to nanoseconds.

2.4. Summary

This chapter aimed to introduce the theory behind the experimental methods and analysis used in the research performed in this dissertation. Specifically, I reviewed the current understanding of the correlation between structural and electronic behavior upon ultrafast laser excitation. Three main areas were covered: nonlinear optics with a focus on second harmonic generation, electronic band structures of direct band gap semiconductors, and relaxation processes of photoexcited semiconductors. These topics are related in that they involve linear and nonlinear subpicosecond optical responses in III-V semiconductors excited above the band gap. These underlying physical processes contribute heavily to answering the research questions reviewed in Chapter 1. In the following chapter, I present the motivations as well as the experimental and analytical methods for the research performed in Chapters 4 and 5.

Chapter 3

Previous Work and Study Justification

In this dissertation, my goal was to further understand correlated structural and electronic behavior upon ultrafast laser excitation. The underlying physical processes described in the previous chapter contribute heavily to answering the research questions from Chapter 1. In this chapter, I provide an experiment-specific framework for characterizing the static and transient nonlinear optical behaviors observed in III-V semiconductors.

This chapter is organized as follows. Section 3.1 presents a project summary and a statement of broader impact. It thus provides an overview of the research performed in this dissertation and motivates the research into static and transient nonlinear optical responses in III-V semiconductors. Next, Section 3.2 reviews the relevant literature in three areas: SHG from unstrained surfaces, SHG from strained semiconductors, and transient SHG spectroscopy of photoexcited semiconductors. This review relates the dissertation project to the state of the field.

Sections 3.3 and 3.4 summarize the objectives and aims as well as the experimental methods used in this dissertation project. Section 3.3 is devoted to outlining Study 1, the study of polarization-resolved second-order nonlinear optical responses of various III-V semiconductor architectures resulting from strain, defect-conducive growth conditions, and substrate choice. Along that same vein, Section 3.4 highlights the methods and objectives of Study 2, which relates the ultrafast PRSHG response of GaAs (100) as a function of transient interatomic potentials within the first picosecond after photoexcitation. Finally, the chapter concludes with a summary of research questions in Section 3.5.

3.1. Overview

Project Summary

There is a large body of materials research on the connection between second order nonlinear optical responses of semiconductors and lattice behavior. The research on second harmonic generation (SHG) on semiconductors largely ignores an important factor related to experimental analysis: input polarization angle. The existing research on the factors influencing SHG in crystalline semiconductors suggest that analyses of SHG spectra are largely driven by the assumption concerning which nonlinear optical susceptibility tensor elements contribute the most to the

resultant SHG. Previous analyses of crystalline materials have previously assumed that the same susceptibility tensor elements contribute to the SHG no matter what the input polarization angle. However, in bulk crystalline materials, this assumption cannot be kept.

It is possible that for the surface of crystalline materials, different tensor elements contribute separately to output SHG intensity depending on input polarization angle. However, it is unclear whether this dependence on polarization angle is sensitive to optically-induced variations on a crystalline surface after photoexcitation. Tensor analysis relates the influence of polarization angle on SH intensity while demonstrating an apparent change in amplitude is, in fact, a change in symmetry.

In addition, surfaces under various conditions (i.e., strain, band bending) may have different SHG responses depending on input polarization angle and therefore display differing symmetries. Thus, it is unclear how variations in semiconductor surfaces influence the nonlinear optical responses at various input polarizations. Also, it is not known how subpicosecond lattice symmetry changes transient nonlinear optical responses, such as transient SHG.

The research in this dissertation attempts to determine the specific factors that influence SHG in crystalline semiconductors. Study 1 investigates whether lattice distortions can accurately be modeled by changes in the nonlinear optical susceptibility tensor components. Several variables related to lattice distortion include strain and interfacial band bending. The results of this study help determine which tensor elements, interatomic potentials, and dipole populations are sensitive to different types of lattice distortions. Study 2 investigates the light-matter interactions undergoing femtosecond excitation. This study extracts transient changes in the susceptibility tensor elements and relates them to their respective dipole populations and interatomic potentials.

Broader Impact

The research of this dissertation represents an initial exploration of the factors influencing nonlinear optical responses on semiconductor surfaces. The results of this research have the potential to inform the field of nonlinear optics about which lattice behaviors are most likely to contribute to static and transient SHG. This information may allow for future work to focus on the connection between SHG, dipole contributions, and

interatomic potentials in semiconductors under different conditions. This research also provides information about whether strain, resonances, and subpicosecond lattice behaviors can be fit with a simple analytical solution. Since the results of this research reveal that an analytical fit of polarization-resolved SHG is sensitive to interatomic potential and dipole variations in all three dimensions simultaneously, this may suggest the need for improved fitting for other semiconductors as well as the need for increased study of other materials.

3.2 Relation of Dissertation Project to the State of the Field

Nonlinear optical spectroscopy has been used to characterize order at crystalline surfaces. Currently, both transient and static second harmonic generation (SHG) spectroscopy techniques are becoming increasingly common tools in describing surface order. While reviewing the literature of SHG from crystalline surfaces, I found there to be limited research into difficulties in describing surface bond interatomic potential and dipole population contributions to resultant SHG intensities from III-V semiconductors. The purpose of this literature review is to report the state of the field and provide context related to the research presented in this dissertation. The following three main challenges to quantifying surface bond contribution to SHG emerged from the literature: SHG from unstrained III-V surfaces, SHG from strained III-V semiconductors, and transient SHG from III-V semiconductors.

Overall, it is evident that the characterization of surface interatomic potentials' contributions to nonlinear optical responses can be a challenge. In fact, providing quantitative understanding of transient nonlinear contributions can be problematic when implementing current phenomenological models of transient SHG. As a result, it is evident that a complete analytical fit is pertinent to overcome the challenges presented by both transient and static SHG characterization of III-V semiconductor surfaces.

SHG from unstrained surfaces

The analysis of SHG spectra from semiconductors can pose a significant challenge to researchers. While microscopic crystal structures can be deduced from rotational azimuthal SHG (RA-SHG) measurements, little has been understood about which interatomic potentials dominate nonlinear responses. Consequently, extracting these contributions from SHG data motivated the development of several bond and field models. In this section, I review the major

developments in this area and provide context for the analysis derived in this dissertation.

In 1987, Sipe et al[14] developed a phenomenological model for silicon to extract macroscopic field information from SHG measurements. The model includes contributions from electric dipoles, electric quadrupoles, and magnetic dipoles at the surface and bulk. This was the first study that employed the analytical use of input-output polarization experimental parameters to separate surface and bulk contributions from each other. The study found that as a result of restricting input and output SHG polarizations, one could quantify possible contributions related to relevant geometry arguments. These contributions were directly relatable to easily fitted Fourier coefficients. With this, it is possible to infer physical insight into the origins of the nonlinear optical responses in silicon.

However, this approach does not generalize well to other materials and had significant limitations. For instance, only the contributions from a centrosymmetric material were considered. For noncentrosymmetric materials like III-V semiconductors, an entirely new method would need to be created. While the model was found to correlate well with silicon surfaces, it was unable to include microscopic variations such as vicinal surfaces and a new model to include this was developed.[15]

Similar to Sipe et al[14], Powell et al[16] produced an analytical model to describe dipole radiation contributions to SHG. The aim of the study was to directly connect the observed macroscopic nonlinear responses to microscopic bond charge behaviors. The researchers sought to achieve this by condensing all fields to only 4 bonds, or a simplified bond hyperpolarizability model (SBHM). While it provided an accurate and simpler physical understanding, this model had significant limitations. For instance, a perfect bulk crystal could easily be described with only 4 repeating bonds. However, surfaces, dangling bonds, vicinal surfaces and strained surfaces cannot. In fact, an incredible amount of numerical computations considering a variety of defects would be required in order to do so. This study also shares the silicon specificity of the Sipe et al[14] phenomenological study. In order to expand the simplified bond model for other materials, one would need to return to first principles.

Interestingly, Germer et al[17] developed a phenomenological model for GaAs relating SHG to the depletion electric field. This model consisted of three terms: dipole bulk contributions as well as first- and second-order depletion field contributions. This

model was compared to experimental RA-SHG of doped GaAs(100) surfaces for a range of input energies. Of the three contributions, the first-order depletion field was the greatest contribution to SHG in GaAs. The fit from this model correlated significantly to the experimental data. However, due to only considering three polarization combinations (p_{in}/p_{out}, p_{in}/s_{out}, and s_{in}/p_{out}) in the model, various effective $\chi_{ijk}^{(2)}$ tensor elements were ignored. Therefore, a limitation of the study is that it does not produce a complete picture of interatomic potential or dipole behavior that would be engaged with other polarization combinations. Nonetheless, a strength of this study is that a significant gap in the literature was identified; the contribution of depletion field to nonlinear optical responses.

In order to address these limitations, Park, Tolk et al[18] developed a polarization-resolved phenomenological model to extract macroscopic field information from SHG measurements of silicon. This was the first study that employed a tensor formalism to extract $\chi_{ijk}^{(2)}$ tensor elements from PRSHG experimental data. The study found that it was possible to quantify (what contributions?) contributions with relevant geometry arguments. With this, they inferred physical insight into the origins of the nonlinear optical response in cubic centrosymmetric crystals like silicon. While the model assumed only a dipole radiation contribution to the PRSHG, it was found to closely fit the experimental data.

In summary, the literature suggests that an analytical model relating polarization-resolved nonlinear optical responses and electric fields is pertinent in the characterization of semiconductors. However, no model has been shown in the literature that can relate most of the 27 $\chi_{ijk}^{(2)}$ tensor elements to the SHG data in III-V semiconductors like GaAs. Consequently, it is imperative that such model can be demonstrated and aim to characterize this and other types of crystalline materials.

SHG from strained semiconductors

Currently, there is a growing use of nonlinear spectroscopic techniques such as SHG to non-destructively characterize strained semiconductors for optoelectronic applications. While it is a widely-researched topic, I found there to be limited research on surface electric field behavior of semiconductors under strained conditions. Consequently, the purpose of this section is to explore the current state of the field and outline the challenges related to the surface (electric) field determination of strained semiconductors.

In a theoretical study, Lyubchanskii et al [19] identified two types of strain that influence SHG of a strained semiconductor film. Specifically, they developed a phenomenological model that relates lattice misfit strain and misfit dislocation strain to a material's $\chi_{ijk}^{(2)}$ effective tensor components. Lattice misfit strain is a lateral strain defined as the ratio of a difference in lattice constants of a film (a_f) and substrate (a_s) to the lattice constant of the substrate (a_s). This misfit can be calculated by the following relation:

$$f = (a_f - a_s)/a_s$$

However, misfit dislocation strain cannot be as easily related to the lattice constant. Instead this type of strain depends on the thickness of the strained film as well. For films less than a material specific parameter known as the critical thickness, there are almost no dislocations. However, for films greater than the critical thickness, there is dislocation strain both along and normal to the surface. For GaAs, the critical thickness is around 30 nm.

Both types of strain contribute to the SHG of a strained film. To distinguish between the different contributions, the Lyubchanskii group postulated that these two types of strain can be separated by polarization analysis of the scattered light (i.e. by using specific probe output polarization angles). The effective $\chi_{ijk}^{(2)}$ tensor elements most sensitive to a dislocation strain can be observed with s-output SHG. On the other hand, p-output SHG was calculated to be sensitive to both dislocation and misfit strain types.

Further evidence to support this approach to strained materials was experimentally verified by Jeong et al[20]. This study measured SHG from a strained piezoelectric film. The aim of the study was to identify and separate the lattice mismatch strain contribution to SHG from electric polarization in the strained piezoelectric film. The study highlighted the extraction of 3 $\chi_{ijk}^{(2)}$ tensor components and photoelastic tensor elements from the RA-SHG data. This study, however, did have some limitations. Due to the small number of tensor elements, one cannot generalize the findings to the entire $\chi_{ijk}^{(2)}$ tensor. But the study did identify a gap in understanding and suggested further studies that are necessary to consider the association of strain and SHG intensities along different input polarization angles.

Similar to Jeong et al[20], Sun et al[21] and Tahini et al[22] discussed the importance of developing a theoretical picture for strain effects in crystalline semiconductors. Specifically, this study focused on three different semiconductors of particular importance to the CMOS industry: Si, Ge, and GaAs. The aim of the study was to provide a detailed investigation of strain altered band structures. This study highlighted that strain affects the band structures with deformation potentials in the conduction and valence band valleys. Consequently, such band distortions drastically affected carrier mobilities. For instance, GaAs was shown to have lower electron mobility and enhanced hole mobility by a factor of 10. These two factors affect carrier screening of the surface. This study, however, did have some limitations. Namely, the changes in the band structure did not translate directly to changes in nonlinear optical responses such as SHG. Nevertheless, this study did identify how strained III-V semiconductors change electronically which could possibly be exploited with resonant SHG measurements near the deformed band edges of strained materials.

Similar to Lyubchanskii et al[19,23] and Jeong et al[20], Schriver et al[24] discuss the importance of SHG in characterizing strained semiconductor thin films in their review article. Specifically, the review describes a potential for effectively characterizing different types of strain in silicon. The review suggests that any analytical model that can characterize the surface field behavior might apply to understanding the structural symmetry of strained silicon. The review found that relating material behavior to nonlinear optical responses could potentially lead to expanding the capabilities of strained silicon.

In summary, the literature suggests that an analytical fit relating nonlinear optical and electric field behavior is pertinent in the characterization of strained semiconductors. However, no model has been shown in the literature that can relate most of the 27 $\chi_{ijk}^{(2)}$ tensor elements to the SHG data in strained semiconductors. Consequently, it is imperative that such a model can be demonstrated.

Transient SHG spectroscopy of photoexcited semiconductors

The analysis of transient SHG spectra from semiconductors can pose a significant challenge to researchers studying ultrafast photoinduced changes. While microscopic crystal structures can be deduced from transient SHG measurements, little has been understood about which field and bond contributions dominate such nonlinear responses. Consequently, extracting contributions from

SHG motivated the development of several transient SHG experiments and analyses.

Understanding lattice dynamics with femtosecond time-resolved SHG can pose another significant challenge. Namely, changes in the linear dielectric function and the electron temperature after excitation are evident in transient SHG responses[25,9,26] in metals after 2 ps. Consequently, semiconducting materials have slower heating timescales, which slows SHG contribution from the photo-induced changes in the linear dielectric function. In this section, I review the major developments in transient SHG in semiconductors and provide context for the work in this dissertation.

In a quantitative study, Nelson et al[27] identified difficulties in characterizing ultrafast interfacial charge transfer at semiconductor interfaces. Time-resolved SH rotational anisotropy spectra for GaAs interfaces were performed at various temperatures. The study did not produce a direct model relating bond polarization, interatomic potentials, or dipole populations, but it did reveal a change in symmetry around SH wavelength of 410 nm. The study suggests that for effective probing of charge carrier dynamics of III-V semiconductor surfaces, forming an experimental-theoretical relationship between SH and ultrafast charge dynamics is imperative. This study further suggests that transient SH phase can be of great importance and incorporation in an analytical fit, thereby allowing characterization of long-lived surface fields. However, the study found that competing frequency-domain interferometric SH (FDISH) and electric field induced second harmonic (EFISH) intensities also contribute strongly to transient rotational azimuthal (RA-SHG) intensities. As a result, there was no determination of transient changes of surface bond polarizations, interatomic potentials, or dipole contributions after photoexcitation.

Further evidence to support the relevance of ultrafast SHG spectroscopy to characterize surface dynamics of III-V semiconductors was identified by Chang et al[28]. The aim of this study was to provide an experimentally verified general theory that describes how pump-induced displacements of surface atoms (or phonons) can be accurately detected with time-resolved SHG. This study highlighted that up to four pump-induced phonon mechanisms are responsible for changes in transient SHG. In the first mechanism, the pump pulse increases carrier density and the atoms are excited into new equilibrium positions. The newly-displaced atoms modify interatomic potential which is sensitive to SHG spectroscopy. A second mechanism is that excited carriers screen the built-in surface electric field, which in turn induces atomic

displacement. The third mechanism is sensitive to the crystal orientation and the pump polarization. It is related to the coherent vibrations in free molecules and molecular crystals. The fourth mechanism is the atomic displacement caused by rapid electronic excitation and de-excitation, in which the atoms accelerate when electrically excited.

In summary, the authors observed an ultrafast increase in the SHG intensity for the GaAs (100) surface after photoexcitation and attributed this to rapid carrier-induced screening in the depletion field. The phonon driving mechanisms described earlier contributed to the oscillations found in the transient SHG spectra. Fourier transforms then delineated the periods of these oscillations and highlighted several THz phonon frequencies corresponding to interfacial and bulk phonons[28].

However, without knowledge of the surface construction, assigning bond behavior to transient SH response proves difficult. All vicinal surfaces in this study produced different transient SH spectra. If one were given a material to characterize without knowing the structural information beforehand, it would be difficult to assign SH response to specific atomic behaviors. Moreover, it is not possible generalize the findings to any crystalline material with this model. However, the study did identify a gap in correlating SH and lattice displacement which suggests that further studies should be carried out to consider the association between the two phenomena.

Similar to Chang et al[28], Wilcox et al[29] discussed the relevance of using time-resolved SHG measurements to characterize photoinduced charge transfer. The aim of the study was to resolve the direction of picosecond charge transfer after excitation. They measured TRSHG intensity and phase as a function of time after pump excitation. This study identified the challenges of reducing stray light and enhancing sensitivity. The method they used was a heterodyne detection scheme which has the advantage of reduced noise and detector dark current. In such a measurement, the phase of a transient signal of one wavelength is compared to the phase of a reference beam of another wavelength. The phase offset provides information about transient changes in the sample material.

However, this type of measurement has several limitations. Phase-based heterodyned measurements cannot be used to extract $\chi_{ijk}^{(2)}$ tensor components without polarization rotation resolution. Another limitation becomes more evident in birefringent materials, which may have different ordinary and extraordinary refractive

indices depending on the wavelength. This restricts the application of this method to materials that do not display large wavelength dependences on refractive indices. Finally, this type of measurement requires comparing phase changes, which may be small in reflective transient SHG measurements. Nonetheless, a strength of this study is that a significant gap was highlighted relating changes in transient SHG to ultrafast interfacial processes.

Interestingly, Park et al[30] extended transient SHG measurement and analysis to probe organic semiconductor thin films. The aim of this study was to observe photoinduced charge separation dynamics in organic semiconductor thin films. The researchers sought to achieve this by observing time-resolved SHG responses. They found that the transient electric field perpendicular to the film surface interacts with the already existing surface space charge field present before irradiation. In addition to providing an accurate and simple physical understanding of photoexcited polymers, this model further demonstrated the versatility of a time-resolved nonlinear optical spectroscopy method to characterize surface dynamics.

In summary, the literature suggests that an analytical fit relating time-resolved nonlinear optical responses and transient electric field behavior is pertinent in the characterization of semiconductors. However, a model has not been shown in the literature that can relate more than 3 $\chi_{ijk}^{(2)}$ tensor elements to the subpicosecond transient SHG response. Consequently, it is imperative that such a model can be demonstrated and aim to characterize III-V semiconductors as well as other types of crystalline materials.

3.3. Study One: Influence of static lattice distortions on polarization resolved SHG

Objectives and Specific Aims

The goal of Study 1 was to assess static surface fields in semiconductors undergoing various types of distortions. One key piece of this assessment is the relationship between distorted surface fields and static nonlinear optical responses. In previous studies, this relationship has been interpreted as either changes in the lattice symmetry through only one bulk $\chi_{ijk}^{(2)}$ tensor component. However, existing experimental and analytical methods do not provide sufficient means of quantifying interrelated contributions to SHG. Nor do these methods quantify how lattice symmetry and $\chi_{ijk}^{(2)}$ elements change with respect to static lattice

distortions. Study 1 aims to fill this gap in knowledge by isolating the $\chi_{ijk}^{(2)}$ tensor components that contribute to the static SHG response and symmetries resulting from different lattice distortions.

The major hypothesis to be tested is that different types of static lattice distortions affect lattice symmetry as well as interatomic potentials on the surface of crystalline materials. This hypothesis depends on the extraction of $\chi_{ijk}^{(2)}$ tensor elements from static SHG measurements as a function of input polarization angle. While such extraction has been performed for undistorted free surface crystalline materials previously in the Tolk group[18], it has not been operationalized in previous research. This study introduces an analytical approach that aims to isolate lateral and normal interatomic potential contributions to SHG from their respective $\chi_{ijk}^{(2)}$ elements for distorted crystalline materials. This strategy focuses on the following three objectives:

1. SHG symmetry response as a function of incident polarization angle. The first objective is to extend the characterization method developed in previous studies of Group IV semiconductors that focuses on the observation of polarization-dependent surface symmetry change as a function of incident polarization angle[18]. This extension includes surface contributions of III-V semiconductors.
2. Changes in surface symmetries as a function of distortion type. The second objective is to observe changes in lattice surface symmetries of experimental PRSHG data through distortions like strain and band bending.
3. Changes in lateral and normal electric surface fields as a function of distortion type. The final objective is to describe these fields due to strain and band bending.

Experimental Methods

The polarization-resolved SHG spectroscopy used in this work has been described elsewhere[18] and the setup is shown in Figure 3.1 below. The excitation light source is a tunable (750 nm – 900 nm) 76 MHz Ti:sapphire laser delivering 120 fs pulses with an average power of 1200 mW. The experiments as explained in this dissertation are performed at 800 nm that induces a second harmonic frequency of 400 nm.

The linear polarization of the incident probe beam is continuously rotated by a half-wave plate which is mounted on a

step rotation motor. For each value of φ (the polarization angle relative to the collision plane), a SHG intensity is recorded for a total of 61 angles between 0° and 360°. The SH wavelength of 400 nm was chosen to observe surface behavior, since the escape depth of 400 nm in GaAs is 15 nm. The 400 nm SHG reflected beam is separated from the fundamental (800nm) reflection by a band-pass filter and directed into a photomultiplier tube (PMT) that is connected to photon counter (PC). The SHG intensity is then counted with a photon counter for at least 10 seconds to assure steady-state SHG response. After 10 s collection at a polarization angle, the half waveplate is rotated to a new polarization angle and the process repeats. The SHG relative intensity values used in this study to calculate steady-state surface fields can be considered valid.

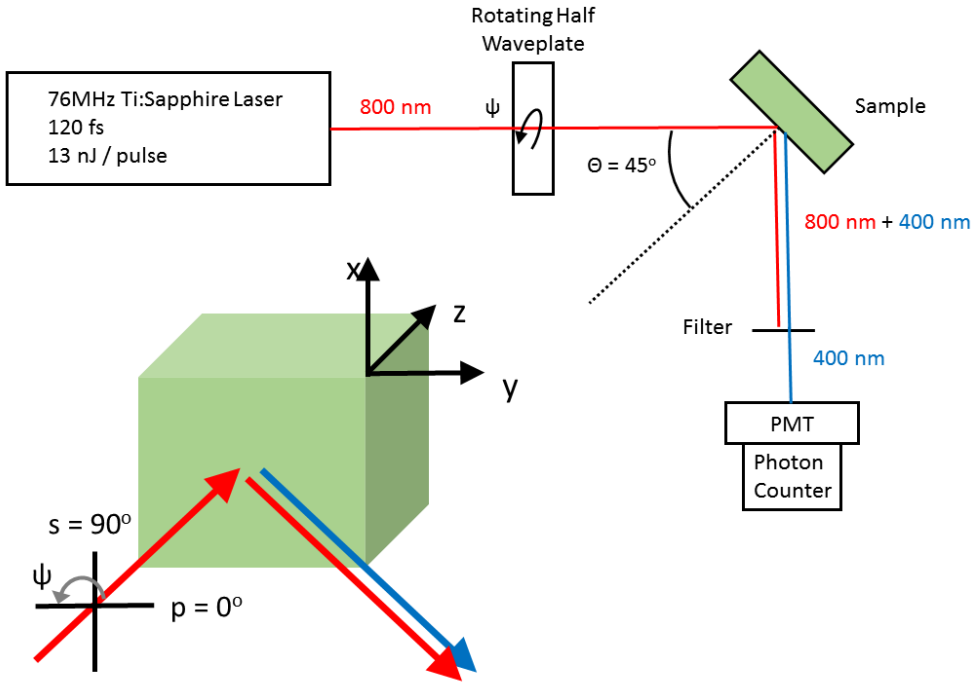

Figure 3.1: Schematic of the setup (a) and sample configuration (b). Probe beam is incident on the sample surface at an incident angle of 45°. Polarization of the probe beam rotates from p-polarization (0° with respect to the collision plane) and s-polarization (90° with respect to the collision plane)

3.4. Study Two: Influence of photoexcitation on time-resolved, polarization-resolved SHG

Objectives and Specific Aims

The goal of Study 2 was to assess the levels of subpicosecond interatomic potential behavior in semiconductors undergoing photoexcitation. One key piece of this assessment is the relationship between ultrafast excitation and changes in the

effective second order nonlinear susceptibility ($\chi_{ijk}^{(2)}$) tensor elements and second harmonic generation (SHG). The relationship has been interpreted as evidence of a sole transient electric field perpendicular to the film surface. However, existing research does not provide sufficient means of quantifying pump-induced changes in SHG due to multiple transient electric fields in several directions simultaneously.

Study 2 aims to fill this gap in knowledge by isolating the $\chi_{ijk}^{(2)}$ tensor components that contribute to multi-directional pump-induced electric fields and transient SHG symmetries. The major hypothesis to be tested is that pump-induced transient electric fields affect variations in transient SHG with respect to input polarization angle. This hypothesis depends on the extraction of $\chi_{ijk}^{(2)}$ tensor elements from transient SHG due to changing incident optical fields as a function of input polarization angle. This extraction of transient SHG based on input polarization has not been operationalized in previous research. This study introduces an analytical approach that aims to isolate transient fields in the *x*, *y*, and *z* directions from their respective $\chi_{ijk}^{(2)}$ elements. This strategy focuses on the following three objectives:

1. Pump-induced symmetry change as a function of time. The first objective is to extend the characterization method developed in Study 1 that focuses on the observation of polarization-dependent surface symmetry change as a function of time.
2. Change in fields as a function of time. The second objective is to apply the analytical model developed in Study 1 in order to describe the transient field behaviors both lateral and normal to the free surface.
3. Decay of transient fields. The final objective is to characterize the decay of lateral and normal transient fields to see if they are anisotropic or isotropic.

Experimental Methods

The transient PRSHG (TR-PRSHG) setup used in this work is similar to the PRSHG setup has been described in the Experimental Methods of Study 1 (Section 3.3). The excitation light source is a tunable 76 MHz Ti:sapphire laser delivering 120 fs pulses with an average power of 1200 mW. This source is split into a pump beam and a probe beam with a 50/50 beam splitter. A retroreflector mounted to a translation stage for the pump beam line delays the time between pump and probe pulses, allowing control of ultrafast

observations. For each value of Δt (the time delay between pump and probe beam pulses) and each value of φ (the probe polarization angle relative to the collision plane), a SHG intensity measurement is recorded for a total of 61 angles between 0° and 360° at 41 time points between -800 fs to 1200 fs.

The 400 nm SHG probe is separated from the 800 nm reflected probe by a band-pass filter and directed into a photomultiplier tube. The total intensity is collected with a lock-in amplifier set to the frequency of the pump beam chopper. The linear polarization of the incident probe beam is continuously rotated in the collision plane by a half-wave plate mounted on a step rotation motor before the sample surface. The linear polarization of the pump beam remains horizontally polarized (p-polarized) throughout the measurement. Finally, the PMT voltage and lock-in settings were adjusted to separate nonlinear optical response to the level of dark current from the PMT and noise level of the lock-in amplifier. The SHG relative intensity values used in this study to calculate steady-state field dynamics can be considered valid.

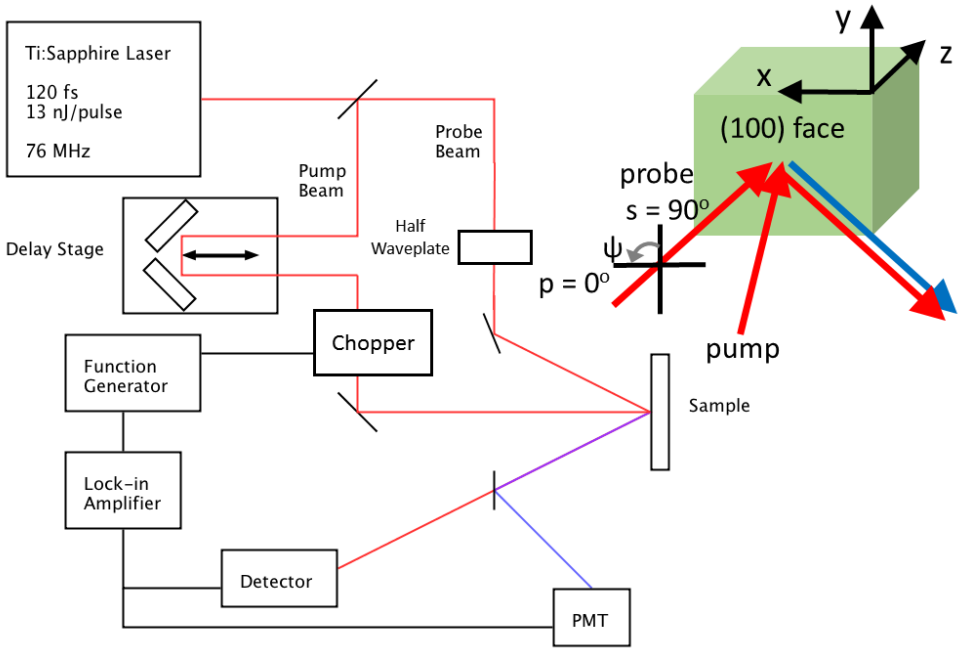

Figure 3.2: Schematic of the setup (a) and sample configuration (b). Probe beam is incident on the sample surface at an incident angle of 45°. Polarization of the probe beam rotates from p-polarization (0° with respect to the collision plane) and s-polarization (90° with respect to the collision plane)

3.5. Summary

Group III-V semiconductors such as gallium arsenide (GaAs) and gallium antimonide (GaSb) as well as the III-V alloy ($Al_xGa_{1-x}As$) were tested due to their strong nonlinear optical responses,

yielding any distinct SHG changes to be clearly seen. The studies utilize a polarization-dependent design. Polarization dependent SHG measurements allow the researcher to explore the main effects of dipole responses with varying the direction of the input optical fields.[18,31] Polarization-dependent or polarization-resolved SHG measurements require fewer alignment changes than the more common rotational azimuthal SHG.

Chapter 4

Polarization-resolved Second Harmonic Generation from Strained and Unstrained III-V Interfaces: Phenomenological Theory and Experiments

4.1 Introduction

Nonlinear optical spectroscopy serves as a valuable characterization method for materials vital to the semiconductor, photovoltaic, and biological sensing industries. One of the most common nonlinear optical characterization methods is second harmonic generation (SHG). This method is particularly sensitive to material symmetries, which are directly related to the electronic structure of materials.

The most common experimental method for SHG characterization is rotational azimuthal SHG (RA-SHG), in which the sample is rotated and the SH intensity is collected as a function of sample azimuthal angle. For years, RA-SHG was successfully employed to characterize Group IV[32,33], Group III-V[34], magnetic[35,36], and strained[23,37,38] semiconductors. In 1987, Sipe, Moss, and van Driel[14] developed a phenomenological model to relate the SHG intensity as a function of sample azimuthal angle to the electric dipole, electric quadrupole, and magnetic quadrupole contributions. Subsequently, this breakthrough became the subject of intensive research in not only centrosymmetric semiconductors[32,39,40], but also nonmagnetic noncentrosymmetric semiconductors[41,42], as well as magnetic[35,42-44] and antiferromagnetic crystals[42,44,45]. For the evaluation in centrosymmetric and noncentrosymmetric materials, the combination of rotational-azimuthal SHG (RA-SHG) and sample-rotation-based phenomenological modeling[14,15,46] has been applied effectively as an indicator of changes in some of the second order nonlinear optical susceptibility tensor elements[14,23,46,47].

However, there is a major limitation intrinsically connected to RA-SHG measurements and associated models. Specifically, the results obtained from these models are only applicable to specific crystal classes. Generally, a separate model is required for each material system. In the cases of strained heterostructures with deformed lattice structures, the model deviates even more from the data and a new model is necessary for each strained configuration. Therefore, such complex system cannot be accurately modeled with a RA-sensitive model. Therefore, it is of great interest to develop experimental and analytical techniques to probe strained semiconductors that are easily extendable to complex systems.

One possible solution is to employ an experimental technique currently used in other contexts. Structural information in biological samples[48–53], nanocrystals[54–56], polymers[57–59], dichalcogenides[60], and noncentrosymmetric surfaces of semiconductors[18,61] can be uncovered by studying the polarization dependence of second harmonic generation (SHG) intensities while keeping the sample stationary. Analytical methods allow the extraction of second-order nonlinear tensor elements from SHG intensities as a function of polarization angle.

This polarization-resolved SHG (PRSHG) experimental method can be exploited to understand steady-state lattice deformation and its effects on associated surface fields, interatomic potentials, and dipole populations of bare and strained semiconductors. In a similar way, PRSHG in combination with a new polarization-resolved phenomenological fit can be used to interpret multilayers as a single effective medium. With this interpretation, it is possible to calculate the relative effective second order nonlinear optical susceptibility tensor elements $\chi_{ijk}^{(2)}$ and probe strain-induced lattice and field modifications. Specifically, a polarization-resolved phenomenological fit can relate contributions of electronic dipole populations and interatomic potentials to PRSHG intensities from specific $\chi_{ijk}^{(2)}$ tensor elements. In this way, the anharmonic potentials contributing to the surface lattice polarization can clearly be visualized without additional sample movement, and so are free from artifacts caused by variations in alignment during rotation.

In this chapter, I use a generalization of second order nonlinear theory along with polarization-resolved experimental techniques to study steady-state lattice polarization on native-oxide covered gallium arsenide (GaAs), low-temperature grown GaAs (LT-GaAs), gallium antimonide (GaSb)/gallium arsenide (GaAs) heterostructures, and gallium antimonide (GaSb)/aluminum gallium arsenide ($Al_xGa_{1-x}As$) heterostructures. By using a polarization-resolved phenomenological fit, I show that it is possible to retrieve the distribution of the static surface electric field, interatomic potentials, and dipole populations from the relative amplitudes of second-order nonlinear optical susceptibility tensor elements. This method uncovers steady-state surface field behaviors that are not visible with conventional rotation azimuthal measurements and related models.

The chapter is organized as follows. Section 4.2 reviews the setup used in this study to obtain p-out and s-out second harmonic intensities as a function of input polarization angle. Also,

included in this section is a description of each sample used in this study. Section 4.3 presents the derivation of the polarization-resolved phenomenological fits which relate PRSHG intensities to specific second order nonlinear optical susceptibility tensor elements. As discussed in Chapter 2, these tensor elements relate directly to interatomic potentials and dipole populations, which give information about the surface lattice polarization. Section 4.4 presents experimental data from the several III-V heterostructures structures along with their respective fits developed in Section 4.3. The major focus of this section is to test the robustness and sensitivity of this fit to various structural configurations of III-V semiconductor interfaces. Finally, the chapter concludes with Section 4.6, which reviews the robustness of this fit and possible applications for further research.

4.2 Methods

Experimental Setup

The polarization-resolved SHG spectroscope used in this work has been described elsewhere[18] and the setup is shown in Figure 3.1 below. The excitation light source is a tunable 76 MHz Ti:sapphire laser delivering 120 fs pulses with an average power of 1200 mW. The incident wavelength is set at 800 nm to generate 400 nm SHG.

The linear polarization of the incident probe beam is then continuously rotated by a half-wave plate that is mounted on a step rotation motor. For each value of φ (the polarization angle relative to the collision plane), a SHG intensity measurement is recorded for a total of 61 angles between 0° and 360°. This SH wavelength was chosen to observe surface behavior, since the escape depth of 400 nm in GaAs is 15 nm. The 400 nm SHG reflected beam is separated from the 800nm reflection by a band-pass filter and directed into a photomultiplier tube (PMT) and photon counter (PC). The SHG intensity is then counted with a photon counter for at least 10 seconds to assure steady-state SHG response. After 10 s collection at a polarization angle, the half waveplate is rotated to a new polarization angle and the process repeats. The SHG relative intensity values used in this study to calculate steady-state surface fields can be considered valid.

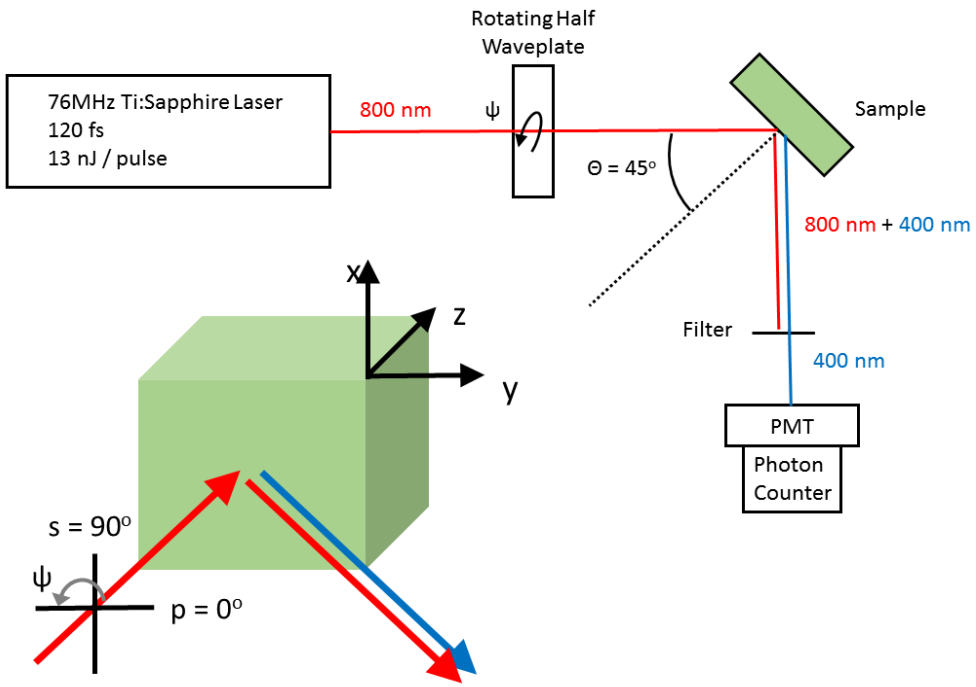

Figure 4.1: Schematic of the setup (a) and sample configuration (b). Probe beam is incident on the sample surface at an incident angle of 45°. Polarization of the probe beam rotates from p-polarization (0° with respect to the collision plane) and s-polarization (90° with respect to the collision plane)

Samples

All samples other than bare GaAs were grown with molecular beam epitaxy (MBE). For these samples, the preparation procedures are described elsewhere[62]. The growth rates and conditions for the various thin films are reviewed below.

20 nm GaSb on GaAs substrate. A 20 nm GaSb film was grown at a growth rate of 800 nm/h on top of a 100 nm undoped GaAs buffer layer. This GaAs buffer layer was first grown on a semi-insulating GaAs (100) substrate at a rate of 750 nm/h.

20 nm GaSb/$Al_xGa_{1-x}As$. A 20 nm GaSb film was grown by MBE with a growth rate of 800 nm/h on top of a 800 nm $Al_xGa_{1-x}As$ (x = 0.27) buffer layer. This AlGaAs layer was grown on a 100 nm undoped GaAs buffer layer at a rate of 800 nm/hr. The GaAs buffer layer was first grown on a semi-insulating GaAs (100) substrate at a rate of 750 nm/h.

400 nm GaSb/GaAs. A 400 nm GaSb film was grown at a substrate temperature of T_s = 490°C at a growth rate of 800 nm/h on top of a 100 nm undoped GaAs buffer layer. This GaAs buffer layer was first grown on a semi-insulating GaAs (100) substrate at a rate of 750 nm/h.

400 nm (low-temperature) LT-GaSb/GaAs. A 400 nm GaSb film was grown at a substrate temperature of T_s = 275°C at a growth rate of 800 nm/h on top of a 100 nm undoped GaAs buffer layer. This GaAs buffer layer was first grown on a semi-insulating GaAs (100) substrate at a rate of 750 nm/h.

4.3 Comprehensive SHG Phenomenological Model

One of the basic concepts in nonlinear optics is to describe contributions to the nonlinear polarization of a material system as a function of the strength of an applied optical field. For second-order nonlinear optical polarization, the analytical procedure is rather straightforward. Typical amplitudes of the second order response are several orders of magnitude smaller than the first order polarization.

Strictly speaking, this enables the applicability of using a power series to describe the superposition of linear and nonlinear contributions to the resultant material's polarization. Furthermore, it makes sense to apply Maxwell's equations to generate an expression for the resultant nonlinear response. It is stipulated by the fact that in the material the nonlinear optical response is a direct result of the unequal charge acceleration in the material. This uneven electronic movement between atoms generates a time-varying polarization which couples to the applied electric field. From this, an analytical solution for fitting polarization-resolved SHG experimental data can be obtained in a straightforward way.

The theoretical development for nonlinear optical response is described in Chapter 2. However, the following point is discussed here in some detail. Let us consider the circumstance in which the applied laser electric field incident upon a nonlinear optical medium. Specifically, the incident laser electric field with frequency ω is described by

$$E(t) = Ee^{-i\omega t} + c.c. \tag{4}$$

The oscillating second order nonlinear polarization $P^{(2)}(t)$ has the form

$$P^{(2)}(t) = \sum_{\mathrm{n}} P(\omega_n)e^{-i\omega_n t} \tag{5}$$

The time-varying portion of that second order nonlinearity has a radiation of wavelength of $2\omega_1$, or twice the incident wavelength ω_1. It is convenient to describe this time-varying polarization as

$$P^2(t) = \sum_{\mathrm{n}} P(\omega_n) e^{-i\omega_n t} = \epsilon_0 \chi^{(2)} E^2(t) \tag{6}$$

The second order nonlinear polarization in a Cartesian direction *i* may be written as a function of the product field amplitudes in the following manner:

$$P_i(\omega_3) = \epsilon_0 \sum_{jk} \chi^{(2)}_{ijk}(\omega_3, \omega_1, \omega_1) E_j(\omega_1) E_k(\omega_1) \tag{7}$$

with

$$d_{il} = \frac{1}{2} \chi^{(2)}_{ijk} \tag{8}$$

where $\chi^{(2)}_{ijk}$ is the second-order susceptibility tensor and *ijk* are Cartesian field components.

Since the focus of this study is on crystalline materials, symmetry conditions and Kleinman contracted notation (d_{ijk}) can further simplify the above expression. Additionally, the SHG response further simplifies the $\chi^{(2)}_{ijk}$ tensor since the input fields in the *j* and *k* directions are of the same wavelength ω_1, making the two indices interchangeable. Thus, Kleinman symmetry condition simplifies *j* and *k* into a combined *l* direction shown in the table below, where 1, 2, and 3 are x, y, and z Cartesian directions, respectively.

jk:	11	22	33	23,32	31,13	12,21
l:	1	2	3	4	5	6

Such notation contracts the third rank $\chi^{(2)}_{ijk}$ tensor into the following two-dimensional matrix d_{il}

$$d_{il} = \begin{pmatrix} d_{11} & d_{12} & d_{13} & d_{14} & d_{15} & d_{16} \\ d_{21} & d_{22} & d_{23} & d_{24} & d_{25} & d_{26} \\ d_{31} & d_{32} & d_{33} & d_{34} & d_{35} & d_{36} \end{pmatrix} \tag{9}$$

Therefore, the total second order polarization in the *x*, *y*, and *z* directions can be expressed as the matrix equation below

$$P(2\omega_1) = \begin{pmatrix} P_x \\ P_y \\ P_z \end{pmatrix} = 2\epsilon_o \begin{pmatrix} d_{11} & d_{12} & d_{13} & d_{14} & d_{15} & d_{16} \\ d_{21} & d_{22} & d_{23} & d_{24} & d_{25} & d_{26} \\ d_{31} & d_{32} & d_{33} & d_{34} & d_{35} & d_{36} \end{pmatrix} \begin{pmatrix} E_{xx} \\ E_{yy} \\ E_{zz} \\ 2E_yE_z \\ 2E_xE_z \\ 2E_xE_y \end{pmatrix} \tag{10}$$

$$= 2\epsilon_o \begin{pmatrix} d_{11}E_{xx} + d_{12}E_{yy} + d_{13}E_{zz} + 2d_{14}E_yE_z + 2d_{15}E_xE_z + 2d_{16}E_xE_y \\ d_{21}E_{xx} + d_{22}E_{yy} + d_{23}E_{zz} + 2d_{24}E_yE_z + 2d_{25}E_xE_z + 2d_{26}E_xE_y \\ d_{31}E_{xx} + d_{32}E_{yy} + d_{33}E_{zz} + 2d_{34}E_yE_z + 2d_{35}E_xE_z + 2d_{36}E_xE_y \end{pmatrix}.$$

A crystal's symmetry can also further simplify the polarization matrix, P_{NL}. The periodic order in crystalline materials ensures that the interaction of the three electric fields (two incident fields and one resultant field) cancel each other, rendering certain d_{il} matrix elements zero. This topic will be reviewed in Sections 4.3.1 and 4.3.2. Below is a table which denotes the nonzero tensor elements for each of the 32 crystal classes.

Crystal System	Crystal Class	Nonvanishing Tensor Elements
Triclinic	$1 = C_1$	All elements are independent and nonzero
	$\bar{1} = S_2$	Each element vanishes
Monoclinic	$2 = C_2$	$xyz, xzy, xxy, xyx, yxx, yyy, yzz, yzx, yxz, zyz,$ zzy, zxy, zyx (twofold axis parallel to $\hat{y}$)
	$m = C_{1h}$	$xxx, xyy, xzz, xzx, xxz, yyz, yzy, yxy, yyx, zxx,$ zyy, zzz, zzx, zxz (mirror plane perpendicular to $\hat{y}$)
	$2/m = C_{2h}$	Each element vanishes
Orthorhombic	$222 = D_2$	$xyz, xzy, yzx, yxz, zxy, zyx$
	$mm2 = C_{2v}$	$xzx, xxz, yyz, yzy, zxx, zyy, zzz$
	$mmm = D_{2h}$	Each element vanishes
Tetragonal	$4 = C_4$	$xyz = -yxz, xzy = -yzx, xzx = yzy, xxz = yyz,$ $zxx = zyy, zzz, zxy = -zyx$
	$\bar{4} = S_4$	$xyz = yxz, xzy = yzx, xzx = -yzy, xxz = -yyz,$ $zxx = -zyy, zxy = zyx$
	$422 = D_4$	$xyz = -yxz, xzy = -yzx, zxy = -zyx$
	$4mm = C_{4v}$	$xzx = yzy, xxz = yyz, zxx = zyy, zzz$
	$\bar{4}2m = D_{2d}$	$xyz = yxz, xzy = yzx, zxy = zyx$
	$4/m = C_{4h}$	Each element vanishes
	$4/mmm = D_{4h}$	Each element vanishes
Cubic	$432 = O$	$xyz = -xzy = yzx = -yxz = zxy = -zyx$
	$\bar{4}3m = T_d$	$xyz = xzy = yzx = yxz = zxy = zyx$
	$23 = T$	$xyz = yzx = zxy, xzy = yxz = zyx$
	$m3 = T_h, m3m = O_h$	Each element vanishes
Trigonal	$3 = C_3$	$xxx = -xyy = -yyz = -yxy, xyz = -yxz, xzy = -yzx,$ $xzx = yzy, xxz = yyz, yyy = -yxx = -xxy = -xyx,$ $zxx = zyy, zzz, zxy = -zyx$
	$32 = D_3$	$xxx = -xyy = -yyx = -yxy, xyz = -yxz,$ $xzy = -yzx, zxy = -zyx$
	$3m = C_{3v}$	$xzx = yzy, xxz = yyz, zxx = zyy, zzz, yyy = -yxx =$ $-xxy = -xyx$ (mirror plane perpendicular to $\hat{x}$)
	$\bar{3} = S_6, \bar{3}m = D_{3d}$	Each element vanishes
Hexagonal	$6 = C_6$	$xyz = -yxz, xzy = -yzx, xzx = yzy, xxz = yyz,$ $zxx = zyy, zzz, zxy = -zyx$
	$\bar{6} = C_{3h}$	$xxx = -xyy = -yxy = -yyx,$ $yyy = -yxx = -xyx = -xxy$
	$622 = D_6$	$xyz = -yxz, xzy = -yxz, zxy = -zyx$
	$6mm = C_{6v}$	$xzx = yzy, xxz = yyz, zxx = zyy, zzz$
	$\bar{6}m2 = D_{3h}$	$yyy = -yxx = -xxy = -xyx$
	$6/m = C_{6h}$	Each element vanishes
	$6/mmm = D_{6h}$	Each element vanishes

Table 4.1: Form of the second-order susceptibility for each of the 32 crystal classes. Each element is denoted by its Cartesian indices. Source: Boyd[13]

Moving to the experimental configuration, the electric field components E_x, E_y, and E_z for a laser with an incident angle θ are

$$E(\psi) = \begin{pmatrix} E_x \\ E_y \\ E_z \end{pmatrix} = \begin{pmatrix} E\cos\theta\cos\psi \\ E\sin\psi \\ E\sin\theta\cos\psi \end{pmatrix} \quad (11)$$

where E is the amplitude of the electric field and ψ is the laser polarization with the convention that the polarization horizontally-oriented with respect to the collision plane is p-polarized (0°) and vertically-oriented is s-polarized (90°) as shown in Figure 3.1.

The dependence of the PRSHG intensity is general and can be expanded to any incident angle, any output PRSHG polarization, and any crystal structure. In this case, the effect of input polarization angle on the generated harmonic intensities can be deduced with setting the incident angle and the collected polarization output angle collected by the PMT.

In this study, I separately collect in two configurations: p-out (0°) and s-out (90°). The contributions to the SHG outputs in p- and s-polarization outputs arise from different second-order nonlinear optical susceptibility tensor elements. The contributions of the tensor elements differ in their expressions because of their geometries. For both the p- and s-polarization outputs, the macroscopic PRSHG intensity as a function of input polarization angle (ψ) can be written in terms of the contracted Kleinman matrix elements.

Of the two collected polarizations, I first turn the reader's attention to p-polarization or 0° output. The resulting phenomenological models are then evaluated against experimental data of GaAs (100), strained GaSb/GaAs (100), and strained GaSb/AlGaAs. These measurements are complementary and are discussed together.

Output p-polarization

Considering an incident angle θ of 45°, the incident electric field components E_x, E_y, and E_z can be expressed as

$$E(\psi) = \begin{pmatrix} E_x \\ E_y \\ E_z \end{pmatrix} = \begin{pmatrix} \frac{1}{\sqrt{2}} E\cos\psi \\ E\sin\psi \\ \frac{1}{\sqrt{2}} E\cos\psi \end{pmatrix}. \quad (12)$$

For the output p-polarization, only the nonlinear fields in the x and z directions are collected, leading to

$$E(2\omega)_{\psi\to p} = A_x P_x + A_z P_z \tag{13}$$

where $E(2\omega)_{\psi\to p}$ is the amplitude of the p-polarized output SH resultant electric field generated from the fundamental input polarization angle (ψ). From Equations (7) and (10), the electric field expression for the SH p-output yields

$$\begin{aligned} E(2\omega)_{\psi\to p} = {} & A_x E^2 (d_{11}E_{xx} + d_{12}E_{yy} + d_{13}E_{zz} + 2d_{14}E_yE_z + 2d_{15}E_xE_z \\ & + 2d_{16}E_xE_y) + A_z E^2 (d_{31}E_{xx} + d_{32}E_{yy} + d_{33}E_{zz} + 2d_{34}E_yE_z \\ & + 2d_{35}E_xE_z + 2d_{36}E_xE_y) \end{aligned} \tag{14}$$

for any crystal class. With the electric field matrix Eq.(9), the above equation becomes

$$\begin{aligned} E(2\omega)_{\psi\to p} = {} & A_x E^2 \left(\frac{1}{2} d_{11}\cos^2\psi + d_{12}\sin^2\psi + \frac{1}{2} d_{13}\cos^2\psi \right. \\ & \left. + \sqrt{2} d_{14}\cos\psi\sin\psi + d_{15}\cos^2\psi + \sqrt{2} d_{16}\cos\psi\sin\psi\right) \\ & + A_z E^2 \left(\frac{1}{2} d_{31}\cos^2\psi + d_{32}\sin^2\psi + \frac{1}{2} d_{33}\cos^2\psi \right. \\ & \left. + \sqrt{2} d_{34}\cos\psi\sin\psi + d_{35}\cos^2\psi + \sqrt{2} d_{36}\cos\psi\sin\psi\right) \end{aligned} \tag{15}$$

Since the intensity of an electromagnetic field is the square of the electric field, the intensity can be described as

$$I(2\omega)_{\psi\to p} = |E_{\psi\to p}(2\omega)|^2 = \left|B_p\cos^2\psi + C_p\cos\psi\sin\psi + D_p\sin^2\psi\right|^2 \tag{16}$$

where

$$\begin{aligned} B_p &= \frac{1}{2}(d_{11} + d_{13} + d_{31} + d_{33}) + d_{15} + d_{35} \\ C_p &= \sqrt{2}\,(d_{14} + d_{16} + d_{34} + d_{36}) \\ D_p &= d_{12} + d_{32} \end{aligned} \tag{17}$$

For the GaAs (100) surface, which has *mm2* symmetry, only d_{15}, d_{24}, d_{31}, d_{32}, and d_{33} are nonzero elements. In bulk GaAs (100), which has symmetry of 43m, the tensor elements, d_{14}, d_{25}, and d_{36} are equal and nonzero. Together, these simplify the B, C, and D coefficients to

$$B_p = \frac{1}{2}(d_{31} + d_{33}) + d_{15} \tag{18}$$

$$C_p = \sqrt{2}\,(\mathrm{d}_{14} + d_{36})$$
$$D_p = d_{32}$$

To allow for fit tolerances, the above expression was expanded which increased the number of fit coefficients to five, yielding

$$I(2\omega)_{\psi\to p} = H\cos^4\psi + J\cos^3\psi\sin\psi + K\cos^2\psi\sin^2\psi + L\cos\psi\sin^3\psi + M\sin^4\psi \quad (19)$$

where

$$H_p = B_p^2 \quad (20)$$
$$J_p = 2B_pC_p$$
$$K_p = 2B_p\,D_p + C_p^2$$
$$L_p = 2C_pD_p$$
$$M_p = D_p^2$$

Output s-polarization

Following the same scheme, it is possible to derive expressions for the s-polarization output. Equation 10 is modified to describe the s-polarization electric field as

$$E(2\omega)_{\psi\to s} = A_yP_y \quad (21)$$

where $E(2\omega)_{\psi\to s}$ is the amplitude of the resultant SH s-out polarization electric field generated by any ψ fundamental input polarization angle. From this equation, the s-out electric field as a function of input fundamental electric field yields

$$E(2\omega)_{\psi\to s} = A_yE^2(d_{21}E_{xx} + d_{22}E_{yy} + d_{23}E_{zz} + 2d_{24}E_yE_z + 2d_{25}E_xE_z + 2d_{26}E_xE_y) \quad (22)$$

for any crystal class. With the input electric field matrix Eq.(10), the output s-polarized SHG intensity as a function of input fundamental polarization angle is

$$E(2\omega)_{\psi\to s} = A_yE^2(\frac{1}{2}d_{21}\cos^2\psi + d_{22}\sin^2\psi + \frac{1}{2}d_{23}\cos^2\psi + \sqrt{2}d_{24}\cos\psi\sin\psi + d_{25}\cos^2\psi + \sqrt{2}d_{26}\cos\psi\sin\psi) \quad (23)$$

which yields an intensity of the form

$$I(2\omega)_{\psi\to s} = |E_{\psi\to s}(2\omega)|^2 = |B_s \cos^2\psi + C_s \cos\psi \sin\psi + D_s \sin^2\psi|^2 \quad (24)$$

where

$$\begin{gathered} B_s = \frac{1}{2}(d_{21} + d_{23}) + d_{25} \\ C_s = \sqrt{2}\,(d_{24} + d_{26}) \\ D_s = d_{22} \end{gathered} \quad (25)$$

For the GaAs (100) surface, which has *mm2* symmetry, only d_{15}, d_{24}, d_{31}, d_{32}, and d_{33} are nonzero. The bulk of GaAs has 43m symmetry which has only $d_{14} = d_{25} = d_{36}$ as nonzero. Together, these contributions simplify the B, C, and D coefficients to

$$\begin{gathered} B_s = d_{25} \\ C_s = \sqrt{2}\,(d_{24} + d_{26}) \\ D_s = 0\,. \end{gathered} \quad (26)$$

To allow for fit tolerances, the above expression was expanded which increased the number of fit coefficients to five, yielding

$$\begin{aligned} I(2\omega)_{\psi\to s} = {} & H_s \cos^4\psi + J_s \cos^3\psi \sin\psi + K_s \cos^2\psi \sin^2\psi + L_s \cos\psi \sin^3\psi \\ & + M_s \sin^4\psi \end{aligned} \quad (27)$$

where

$$\begin{gathered} H_s = B_s^2 \\ J_s = 2B_sC_s \\ K_s = 2B_sD_s + C_s^2 \\ L_s = 2C_sD_s \\ M_s = D_s^2 \end{gathered} \quad (28)$$

For SHG measurements involving a photomultiplier tube and photon counter combination, an inherent dark current contributes to the SH background signal count. To account for this background count in the model, an extra term $I_{background}(2\omega)$ is included in the fitting equation below

$$I(2\omega)_{\psi\to p,s} = I_{background} + I(2\omega)_{\psi\to p,s} \quad (29)$$

In the case for both p-out and s-out PRSHG responses, the fit coefficients $B_{p/s}$, $C_{p/s}$, and $D_{p/s}$ can be obtained with the following relations:

$$\begin{aligned} |B_{p,s}| &= \sqrt{H_{p,s}} \\ |D_{p,s}| &= \sqrt{M_{p,s}} \\ |C_J| &= \frac{J}{2|B_{p,s}|} \\ |C_L| &= \frac{L}{2|D_{p,s}|} \end{aligned} \tag{30}$$

which can yield nonphysical complex values. To avoid this, I limit the arguments H and M to be greater than or equal to zero. With this limit, the values for B, C, D, and subsequently the $X_{ijk}^{(2)}$ tensor elements are physical.

The tensor element contributions can then be extracted from the p-out and s-out PRSHG data and fit coefficients through Eq. (14), (22), and (27) to produce the relationships in Table 4.2 below.

$X_{ijk}^{(2)}$ **Calculated from Fit Coefficients**	
$\frac{1}{2}(X_{xxx}^{(2)} + X_{zzz}^{(2)} + X_{zxx}^{(2)} + X_{zzz}^{(2)}) + X_{xxz}^{(2)} + X_{zxz}^{(2)}$	$2B_p$
$X_{xyz}^{(2)} + X_{xxy}^{(2)} + X_{zyz}^{(2)} + X_{zxy}^{(2)}$	$\sqrt{2}C_P$
$X_{xyy}^{(2)} + X_{zyy}^{(2)}$	$2D_p$
$\frac{1}{2}(X_{yxx}^{(2)} + X_{yzz}^{(2)}) + X_{yyx}^{(2)}$	$2B_s$
$X_{yyz}^{(2)} + X_{yyx}^{(2)}$	$\sqrt{2}C_s$
$X_{yyy}^{(2)}$	$2D_s$

Table 4.2: Second order nonlinear optical susceptibility tensor elements calculated from fit coefficients

4.4. Results and Discussion

In this work, I implemented polarization-resolved SHG experimental methods and to probe the orientation of the surface lattice polarization on various III-V interfaces. In the following sections, I present the results of the phenomenological fit to the experimental data for III-V free surfaces, defect-heavy thin films, and heterostructures. In this way, relative nonlinear optical susceptibility tensor elements can be effectively modeled with great sensitivity to structure, defects, and strain. However, I ignore resonant nonlinear responses near the band gap. In this

section, I present the applications of this model to four specific samples: (100) GaAs, low-temperature GaAs (100), and GaSb/GaAs and GaSb/AlGaAs heterostructures. The structural parameters of noncentrosymmetric surfaces are often expressed in terms of 27 second-order nonlinear optical susceptibility tensor elements, which relate the SH intensities to specific dominant lattice polarizations. All fits in this study were performed in OriginPro 9.0.

PRSHG of native-oxide GaAs (100)

The p- and s-polarized output PRSHG responses from native-oxide GaAs (100) are presented in Figure 4.2. This figure shows the single beam PRSHG spectra as a function of incident probe polarization angle with 0° (p-polarized) defined as parallel to the collision plane between pump and probe and 90° (s-polarized) defined as perpendicular to the collision plane. For both measurements, the SH intensities were recorded for 61 incident polarization angles between 0° and 360°.

To compare the trends in the p-out and s-out PRSHG data, each data set was normalized to its maximum to remove variation between the spectra during collection. The solid red lines indicate the previously mentioned fits derived in Section 4.3. From this figure, it is clearly seen that the fits (red lines) match closely to both sets of polarization-resolved SHG data.

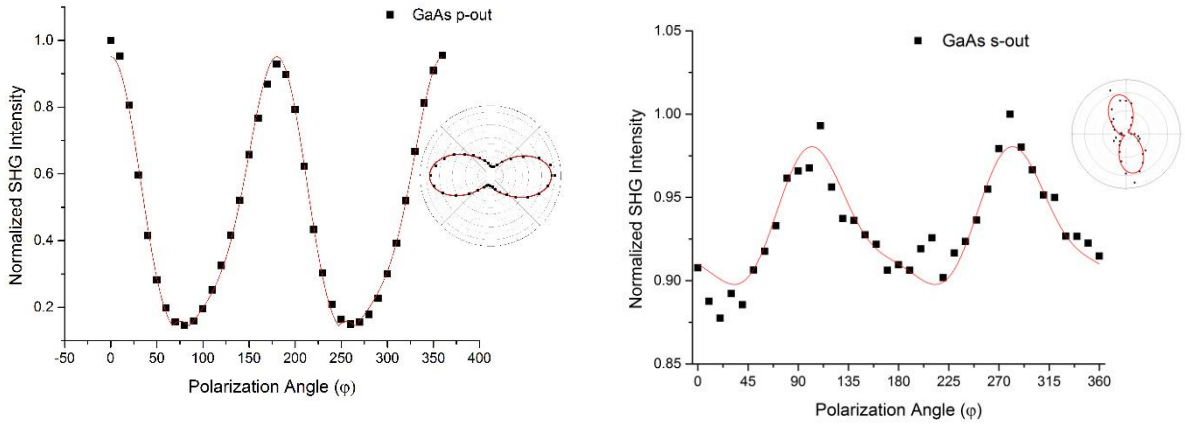

Figure 4.2: PRSHG obtained for native-oxide GaAs (100). The data are shown for p-polarized (0°) output (a) as well as s-polarized (90°) output (b).

From comparing the experimental results of both configurations, it is evident that the material responses are well reproduced by the polarization-resolved phenomenological fit equations (26) and (27) to obtain the fitting coefficients I, B_p, C_p, D_p, B_s, C_s, and D_s given in Equations (16), (24), and (26).

These coefficients for GaAs (100) are shown in Table 4.3. From the fit coefficients in Table 4.3 for GaAs under no external strain, I obtain the $\chi_{ijk}^{(2)}$ tensor elements shown in Table 4.4.

GaAs (100)

	p-out		*s-out*	
Fit from Eq. (26)	H_p	0.004	H_s	0.302
	J_p	-0.115	J_s	-0.024
	K_p	0.402	K_s	0.596
	L_p	0.639	L_s	-0.064
	M_p	0.359	M_s	0.365
	I	0.497	I	0.608
Calculated from Eq. (27)	B_p	0.066	B_s	0.549
	D_p	0.599	D_s	0.605
	C_J	0.870	C_J	0.022
	C_L	0.533	C_L	0.053

Table 4.3: Fit coefficients from Equations 26 and 27 for normalized PRSHG s-out and p-out data on (100) GaAs

The polarization-resolved fit of second order nonlinear optical properties are in good agreement with previous bond-charge and RA-SHG models. The results from the polarization-resolved phenomenological fits to the data reveal that several prominent features of the nonlinear optical responses arise from the combinations of specific tensor elements, and that the effects in the observed SH intensities are small perturbations of these tensor elements. When the $X_{ijk}^{(2)}$ tensor elements from this model are compared to previous work done by others, it is evident that the ones that contribute the most to the PRSHG intensities match those found in the Sipe RA-SHG model for noncentrosymmetric cubic semiconductors. This indicates that, to a good approximation, the extraction of relative $X_{ijk}^{(2)}$ tensor elements are indeed transferable to new geometries and materials.

Calculated from Fit Coefficients		$X_{ijk}^{(2)}$
$2B_p$	0.132	$\frac{1}{2}(X_{xxx}^{(2)} + X_{zxz}^{(2)} + X_{zxx}^{(2)} + X_{zzz}^{(2)}) + X_{xxz}^{(2)} + X_{zxz}^{(2)}$
$\sqrt{2}C_P$	0.992	$X_{xyz}^{(2)} + X_{xxy}^{(2)} + X_{zyz}^{(2)} + X_{zxy}^{(2)}$
$2D_p$	1.198	$X_{xyy}^{(2)} + X_{zyy}^{(2)}$
$2B_s$	1.098	$\frac{1}{2}(X_{yxx}^{(2)} + X_{yzz}^{(2)}) + X_{yyx}^{(2)}$
$\sqrt{2}C_s$	0.0375	$X_{yyz}^{(2)} + X_{yyx}^{(2)}$
$2D_s$	1.210	$X_{yyy}^{(2)}$

Table 4.4: Normalized second order nonlinear optical susceptibility tensor elements for (100) native-oxide GaAs PRSHG s-out and p-out data

PRSHG of low-temperature GaSb on GaAs

In this work, I also utilized the same procedure to probe the orientation of the depletion-field lattice polarization on high-defect low-temperature grown III-V heterostructures, specifically GaSb thin films grown on GaAs substrates. In principle, one should be able to use this method to characterize surface defects caused by growth conditions of semiconductors. Here, I will focus on the consequences that low-temperature growth defects have on PRSHG spectra. The comparison between low-temperature grown GaSb (LT-GaSb) and normally grown GaSb films is illustrated in Figure 4.3. To compare the trends in PRSHG data between the two samples, each data set was normalized to its maximum. This removes sources of alignment variation between SH spectra during collection.

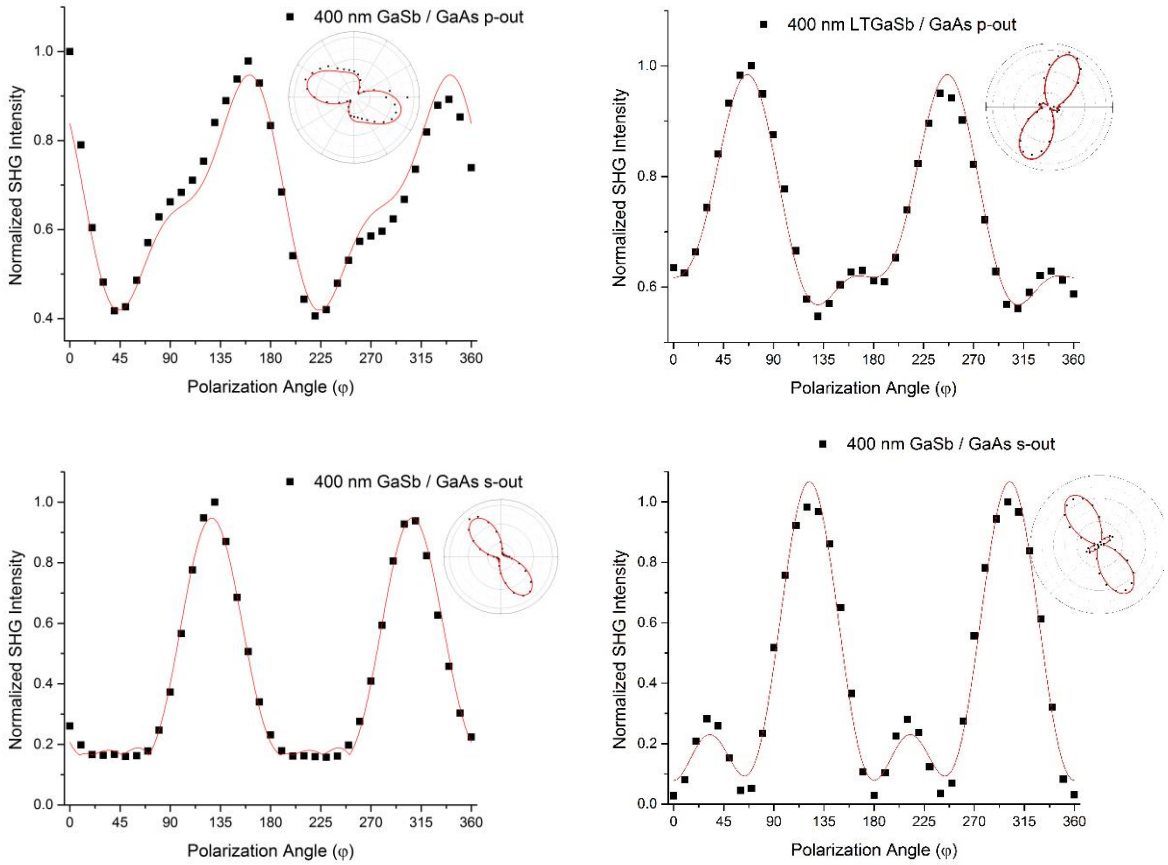

Figure 4.3: PRSHG obtained for (100) 400 nm low-temperature-grown LT-GaSb on GaAs and 400 nm GaSb on GaAs substrate. The data are shown for p-polarized (0°) output (a), (b) as well as s-polarized (90°) output (c),(d).

For 400 nm GaSb and 400 nm low-temperature GaSb films grown on GaAs substrates, Figure 4.3 shows the p-out and s-out PRSHG spectra as well as the phenomenological fits (red lines) to the p-out and s-out PRSHG data for 400 nm LT GaSb/GaAs (a), 400 nm GaSb/GaAs (100) (b) and p-out PRSHG data for 400 nm LT GaSb/GaAs (c), 400 nm GaSb/GaAs(100) (d). The red lines are the fits discussed in Section 4.3 as a function of incident probe polarization angle. To my knowledge, this is the first discussion of all 27 tensor elements from SHG spectra. From this figure, it is evident that there is considerable agreement between the fit and PRSHG responses in all four cases. The fitting coefficients from the model are displayed below in Table 4.5.

LT-GaSb/GaAs Heterostructures

	p-out		
	400 nm GaSb/GaAs		400 nm LT-GaSb/GaAs
Fit from Eq. (26)	H_p	0.420	0.093

	J_p	-0.626	3.092e-4
	K_p	0.142	0.375
	L_p	-0.153	0.597
	M_p	0.213	0.317
	I	0.419	0.524
Calculated from Eq. (27)	B_p	0.648	0.305
	D_p	0.462	0.563
	C_J	0.483	--
	C_L	0.166	0.530
s-out			
Fit from Eq. (26)	H_s	0.042	0.014
	J_s	-0.434	-0.007
	K_s	1.224	1.569
	L_s	-1.052	-1.485
	M_s	0.237	0.395
	I	0.165	0.064
Calculated from Eq. (27)	B_s	0.205	0.120
	D_s	0.486	0.629
	C_J	1.058	0.030
	C_L	1.081	1.181

Table 4.5: Fit coefficients from Equations 26 and 27 for normalized PRSHG s-out and p-out data on 400 nm LT-GaSb/GaAs and 400 nm GaSb/GaAs heterostructures

In order on include defect-induced lattice polarization in the model described earlier, the model includes the defect concentrations as effective $\chi_{ijk}^{(2)}$ tensor elements. Since changes in SHG intensity are proportional to defect density as discussed in previous studies[63,64], one possibly could relate variations in effective $\chi_{ijk}^{(2)}$ tensor elements directly to interatomic potentials and dipole populations affected by defect densities. These results indicate that this experimental and analytical method is well optimized for a description of growth-mediated defects as well as bare surfaces and buried heterointerfaces.

400 nm GaSb/As and LT-GaSb/GaAs Heterostructures

Normalized Effective $X_{ijk}^{(2)}$	400 nm GaSb/GaAs	400 nm LT-GaSb/GaAs
$\frac{1}{2}(X_{xxx}^{(2)} + X_{zxz}^{(2)} + X_{zxx}^{(2)} + X_{zzz}^{(2)}) + X_{xxz}^{(2)} + X_{zxz}^{(2)}$	1.296	0.610

$X_{xyz}^{(2)} + X_{xxy}^{(2)} + X_{zyz}^{(2)} + X_{zxy}^{(2)}$	0.459	0.750
$X_{xyy}^{(2)} + X_{zyy}^{(2)}$	0.924	1.126
$\frac{1}{2}(X_{yxx}^{(2)} + X_{yzz}^{(2)}) + X_{yyx}^{(2)}$	0.410	0.240
$X_{yyz}^{(2)} + X_{yyx}^{(2)}$	1.070	1.670
$X_{yyy}^{(2)}$	0.972	1.258

Table 4.6: Normalized second order nonlinear optical susceptibility tensor elements for PRSHG s-out and p-out data on 400 nm LT-GaSb/GaAs and 400 nm GaSb/GaAs heterostructures

The tensor elements display defect-sensitive responses not only in the p-out PRSHG response but also in the s-output PRSHG response at 3.1 eV. Although the normalized $X_{yyy}^{(2)}$ and $X_{xyy}^{(2)} + X_{zyy}^{(2)}$ tensor elements increase for the low-temperature grown sample, this is counterbalanced by the drastic decrease of the $\frac{1}{2}(X_{xxx}^{(2)} + X_{zxz}^{(2)} + X_{zxx}^{(2)} + X_{zzz}^{(2)}) + X_{xxz}^{(2)} + X_{zxz}^{(2)}$ element group, resulting in marked changes in the PRSHG responses.

For the LT-GaSb film, the s-out PRSHG displays distinct peaks at 30° and 210° that are noticeably absent from the normally grown GaSb film. Therefore, the low-temperature defects cause an enhancement from the normalized $X_{yyy}^{(2)}$ and $X_{xyy}^{(2)} + X_{zyy}^{(2)}$ tensor elements. This varied response could be understood within the context of defect-dependence on low-temperature grown III-V semiconductors. In previous work, such growth conditions were credited to the creation of native point defects, specifically antisite As_{Ga} and gallium vacancies (V_{Ga}) defects. Antisite As_{Ga} and V_{Ga} defect distortions relieve the strain in the low-temperature GaSb[65,66]. The relief of this strain normal to the surface is compensated by lateral strain in the x and y directions. Such compensation increases the value of the y-based tensor elements which manifests in the s-out PRSHG response.

This enhancement is not only observed in the s-out PRSHG. For instance, the p-out PRSHG response displays a noticeable suppression of the peaks at 160° and 340°. The only set of tensor elements undergoing a decrease is $\frac{1}{2}(X_{xxx}^{(2)} + X_{zxz}^{(2)} + X_{zxx}^{(2)} + X_{zzz}^{(2)}) + X_{xxz}^{(2)} + X_{zxz}^{(2)}$, by about half. This set of tensor elements dominates the p-out PRSHG response of as-grown GaSb whereas it is the smallest contribution for the low-temperature grown GaSb. This varied SH response could be understood within the context of defect-sensitivity mentioned earlier with s-out PRSHG. The same antisite As_{Ga} and V_{Ga} defect distortions relieve perpendicular strain in the low-temperature GaSb[65,66]. The relief of this strain normal to the surface is compensated in lateral strain in the y direction. Such

compensation increases the value of the $X_{xyz}^{(2)} + X_{xxy}^{(2)} + X_{zyz}^{(2)} + X_{zxy}^{(2)}$ and $X_{xyy}^{(2)} + X_{zyy}^{(2)}$ to a much greater extent. The model developed in this study appears to be rather sensitive to such defects at fundamental wavelengths above the band gaps of both III-V semiconductors.

PRSHG of GaSb/GaAs and GaSb/AlGaAs heterostructures

Since previous SHG measurements and models have not effectively distinguished resonant electronic contributions in strained semiconductors, I placed special emphasis on obtaining at least one case of band gap distortion in strained III-V semiconductors. To this effect, I implemented polarization-resolved SHG spectroscopy to probe the orientation of the depletion-field lattice polarization on strained III-V heterostructures, specifically GaSb/GaAs and GaSb/AlGaAs bilayers. This is the first discussion of all 27 tensor elements from SHG spectra originating from the surface of buried III-V heterointerfaces.

To test the effect band gap distortion has on nonlinear optical responses, I excited SHG with a fundamental frequency (1.5 eV) between the band gaps of the GaSb film (0.73 eV) and AlGaAs substrate (1.76 eV). If intermediate band structures exist near 1.5 eV, a resonance contribution to the SHG intensity is likely to at the GaSb/AlGaAs heterointerface. Within this context, I find that the dominant interaction of the surface PRSHG response is due to resonant electron contribution from the AlGaAs (27% Al) substrate. To compare the trends in the data between the two samples, each data set was normalized to its maximum. This should remove sources of alignment variation between SH spectra during

collection.

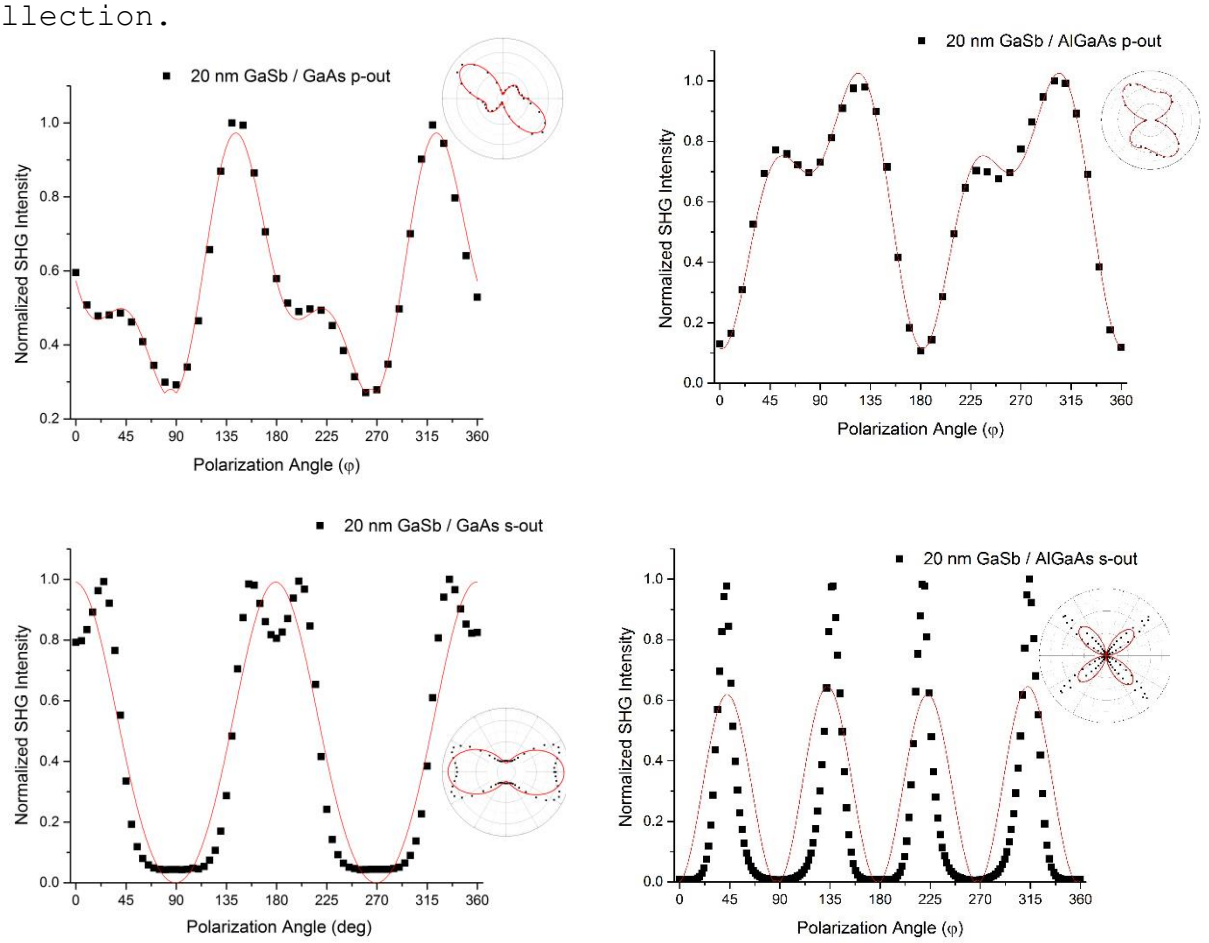

Figure 4.4 PRSHG obtained for (100) 20 nm GaSb on GaAs (a),(c) and 20 nm GaSb on AlGaAs substrate (b),(d). The data are shown for p-polarized (0°) output (a), (b) as well as s-polarized (90°) output (c),(d).

Figure 4.4 shows the result of the phenomenological fit (red lines) to 20 nm GaSb/GaAs s-out (a)and p-out (c) PRSHG data as well as the 20 nm GaSb/AlGaAs s-out (b)and p-out (d) PRSHG data. The fit closely matches spectra structures, of all but Figure 4d. These relate to resonant electronic contributions compounded by effect that strain has have on the band structure. The nonlinear response may be increased in regions of strain and suppressed in regions without strain as shown in the previous sections. To determine which tensor elements are affected, I employ the macroscopic polarization-resolved fit mentioned in the previous sections. These fit coefficients from the normalized PRSHG data of the 20 nm GaSb/GaAs and 20 nm GaSb/$Al_xGa_{1-x}As$ heterostructures are summarized in Table 4.7 below.

20 nm GaSb/GaAs and 20 nm GaSb/$Al_{0.27}Ga_{0.73}As$ Heterostructures

p-out				
	20 nm GaSb/GaAs		20 nm GaSb/$Al_{0.27}Ga_{0.73}As$	
Fit from Eq. (26)	H_p	0.303	0.057	
	J_p	-0.636	-0.134	
	K_p	1.479	2.368	
	L_p	-0.248	-0.368	
	M_p	0.000	0.669	
	I	0.270	0.058	
Calculated from Eq. (27)	B_p	0.550	0.239	
	D_p	0.000	0.818	
	C_J	0.578	0.280	
	C_L	--	0.225	
s-out				
Fit from Eq. (26)	H_s	0.042	--	
	J_s	-0.434	0.183	
	K_s	1.224	2.512	
	L_s	-1.052	-0.235	
	M_s	0.237	--	
	I	0.165	--	
Calculated from Eq. (27)	B_s	0.205	--	
	D_s	0.486	--	
	C_J	1.058	C_k	1.585
	C_L	1.081		

Table 4.7: Fit coefficients from Equations 26 and 27 for normalized PRSHG s-out and p-out data on 20 nm GaSb/GaAs and 20 nm GaSb/$Al_{0.27}Ga_{0.73}As$ heterostructures

From the fit coefficients in Table 4.7 and the relations in Table 4.2, it is possible to determine the 27 second order nonlinear optical susceptibility tensor elements for 20 nm GaSb/GaAs and 20 nm GaSb/AlGaAs heterostructures. These elements are given in Table 4.8 below.

20 nm GaSb/As and GaSb/AlGaAs Heterostructures

	$X_{ijk}^{(2)}$	20 nm GaSb/GaAs	20 nm GaSb/$Al_{0.27}Ga_{0.73}As$
p-out	$\frac{1}{2}(X_{xxx}^{(2)} + X_{zxz}^{(2)} + X_{zxx}^{(2)} + X_{zzz}^{(2)}) + X_{xxz}^{(2)} + X_{zxz}^{(2)}$	1.100	0.478
	$X_{xyz}^{(2)} + X_{xxy}^{(2)} + X_{zyz}^{(2)} + X_{zxy}^{(2)}$	0.817	0.357
	$X_{xyy}^{(2)} + X_{zyy}^{(2)}$	--	1.636
s-out	$\frac{1}{2}(X_{yxx}^{(2)} + X_{yzz}^{(2)}) + X_{yyx}^{(2)}$	0.084	--
	$X_{yyz}^{(2)} + X_{yyx}^{(2)}$	1.512	2.242
	$X_{yyy}^{(2)}$	0.972	--

Table 4.8: Normalized second order nonlinear optical susceptibility tensor elements for PRSHG s-out and p-out data on 20 nm GaSb/GaAs and 20 nm GaSb/$Al_{0.27}Ga_{0.73}As$ heterostructures

From Table 4.8, it is clear that the factors $\frac{1}{2}(X_{xxx}^{(2)} + X_{zxz}^{(2)} + X_{zxx}^{(2)} + X_{zzz}^{(2)}) + X_{xxz}^{(2)} + X_{zxz}^{(2)}$ and $X_{xyz}^{(2)} + X_{xxy}^{(2)} + X_{zyz}^{(2)} + X_{zxy}^{(2)}$ are responsible for the p-out PRSHG signal at 3.1 eV for the 20 nm GaSb/GaAs. The last $X_{ijk}^{(2)}$ relation does not contribute significantly to the PRSHG spectra for this sample. For the s-out PRSHG signal, the $X_{yyz}^{(2)} + X_{yyx}^{(2)}$ contribution is dominant. From these observations, it is clear that the GaSb layer at the interface is considerably strained normal to the interface.

This behavior is in good agreement with RA-SHG experiments on various thicknesses of strained III-V multilayers. For film thicknesses below the critical thickness, it is reported that the distortion caused by the difference in lattice constants creates strains which affect SHG intensities[19,20,23]. Furthermore, other studies have postulated that the strained films form an estimated defect density, which produces increased SHG intensity[63,64]. It is reasonable to speculate that the strained film produces distorted interatomic potentials in the depletion field which is sensitive to PRSHG spectroscopy.

For the 20 nm GaSb/AlGaAs heterostruture, the factor $X_{xyy}^{(2)} + X_{zyy}^{(2)}$ factor contributes the most to the p-out PRSHG intensity as shown in Table 4.8. From this information, one could surmise that the GaSb film is more strained by the AlGaAs substrate than by the GaAs substrate. However, that is not the case. Both 20 nm GaSb films have similar levels of increased strain due to the

differences in lattice constants between GaAs (a = 5.65325 Å), GaSb (a = 6.09593 Å) and $Al_{0.27}Ga_{0.73}As$ (5.65541 Å). Therefore, this lattice mismatch between GaSb and $Al_{0.27}Ga_{0.73}As$ is about the same as the mismatch between GaSb and GaAs, so the strain is not much different between the two heterostructures and would not explain the observed differences between the PRSHG responses.

One explanation for the varied PRSHG responses is resonance behavior. From the discussion in Chapter 2, resonance second harmonic response can be generated when either the fundamental excitation or harmonic response is the same frequency as a level in the band structure. In the case of the GaSb/GaAs heterostructure, the fundamental beam of 1.55 eV is larger than the GaSb band gap (0.726 eV) and the GaAs band gap (1.424 eV). However, the fundamental beam of 1.55 eV falls within the intermediate bands of the strained GaSb/AlGaAs heterostructure. This effect is illustrated below in Figure 4.5. Therefore, this data for the AlGaAs substrate does confirms the statement that the resonant electronic contribution from the subsurface could dominate the nonlinear optical response. In fact, it may have a larger contribution than the interfacial strain.

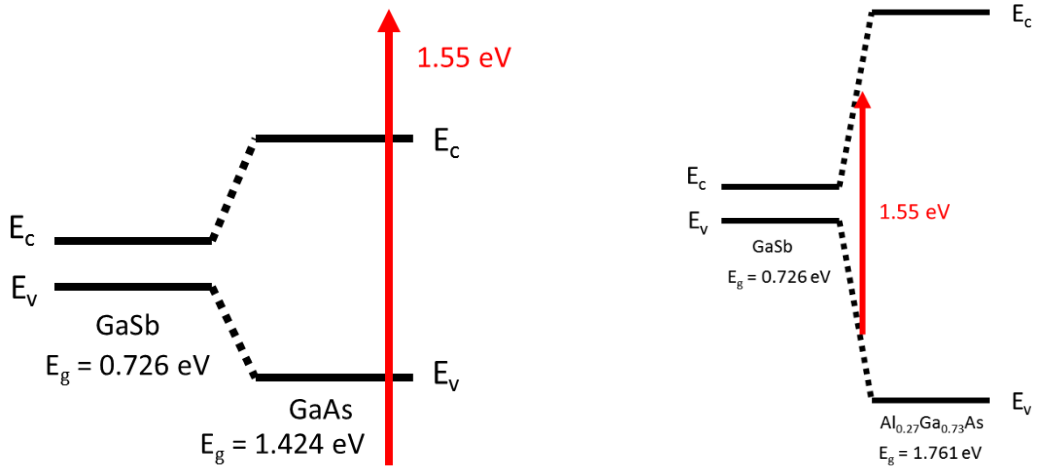

Figure 4.5: Simplified band diagram of interfacial band distortion in III-V semiconductor heterostructures

The model developed in this study cannot readily determine the resonant contributions to nonlinear optical responses. However, based on trends found in this study, I offer suggestions for future work that isolate resonant contributions to PRSHG spectra. For example, one could vary the input fundamental probe frequency to quantitatively study the resonance-related increase of the $X_{yyz}^{(2)} + X_{yyx}^{(2)}$ and $X_{xyy}^{(2)} + X_{zyy}^{(2)}$ tensor elements to understand how the distorted band structure of the GaAs/AlGaAs system contribute to the nonlinear

optical behavior of III-V heterostructures. However, that is beyond the scope of this study but serves as a starting point for future experiments. To summarize, the results clearly show that PRSHG is sensitive not only to strain and vacancy defects but also to the resonant SHG responses of buried III-V semiconductor alloy interfaces.

4.5. Conclusions

In summary, I have applied a polarization-resolved model to study the surface lattice polarizations of free and buried interfaces of III-V semiconductors in three cases. The phenomenological fit developed in this study has been shown to qualitatively reproduce most of the experimental features of the PRSHG spectra from free interfaces, growth-mediated defects, and strained thin films. By fitting the coefficients of this model to the data, it is possible to relate SH intensities to specific interatomic potential changes in the depletion region caused by strain from the relationships between all 27 $\chi_{ijk}^{(2)}$ tensor elements.

However, the model does not account for resonant electronic behavior from the mid-gap GaSb/AlGaAs heterostructure. This suggests that resonant electronic contributions to the PRSHG spectra may not be as easily fit with this method. The sensitivity shown by this model is such that one can refine PRSHG response by varying experimental parameters such as wavelength to induce resonant PRSHG responses. To understand interatomic potentials without the influence of such resonances, the GaAs/AlGaAs sample should be studied at various wavelengths away from the band gap of AlGaAs. However, this is beyond the scope of this chapter. Although the model is not accurate for determining which tensor elements contribute to resonant PRSHG intensities, it provides an appropriate starting point for more detailed models of the PRSHG spectra. More importantly, the primary advantage of this approach is its applicability to both surface and bulk polarizations. In conclusion, such work leads the way to structural quantitative characterization of crystalline materials.

Chapter 5

Characterization of Depletion-Field Dynamics in GaAs by Time- and Polarization-resolved Second Harmonic Generation

5.1 Introduction

Structural field dynamics are key parameters in a large variety of ultrafast optoelectronic phenomena. Polarization-sensitive imaging has been exploited in biology to image *in vivo*[67] and *in vitro* 3D molecular orientation distributions of collagen fibrils[51,68,69], skeletal muscles[70], microtubles[53], and thick tissues[71] among others. Deducing 3D structural information in semiconductors using polarization-resolved second harmonic generation data is the next logical step.

Since the introduction of second harmonic generation (SHG) microscopy in semiconductor imaging, it has been widely used to image disorder from free-surface, buried-surface, micro- and nanopatterned, and ion-implanted[57,72] semiconductors. Coherent SHG occurring naturally at noncentrosymmetric surfaces is currently exploited as a functional opportunity for the development of ultrafast surface optoelectronics. In addition to monitoring atomic distortions native to the material, SHG can also characterize the controllable active distortions of lattice polarizations caused by photoexcitation from a femtosecond laser pulse.

Previously, semiconductors have been imaged through rotational azimuthal second harmonic generation (RA-SHG) based on the use of a phenomenological model dependent on the rotation of the probed sample. Such measurements and models applied to III-V semiconductors, specifically gallium arsenide (GaAs), have shown that the GaAs structure can be reduced to an equivalent material with only 4 tetrahedrally-bonded atoms[73,74]. Many works have developed this bonded model to quantify atomic order in III-V semiconductors from experimental data.

In complex environments, however, such as pump-induced variations in surfaces of III-V semiconductors, more complex behavior is expected. It is imperative to create a model for this behavior. Tentative analyses have been performed in this direction by collecting transient SHG data at one polarization angle.[75] However, these models are incomplete because adding a single ultrafast parameter to the analysis of the nonlinear optical susceptibility tensor elements leads to ambiguous and incomplete

determinations. In addition, these parameters remain dependent on extreme lattice disordering only available through nonthermal and thermal melting at high laser fluences (> 1kJ/m^2).

Finally, the estimation quality of the second order nonlinear optical susceptibility tensor elements strongly depends on the reliability of the SHG measurements, which can be difficult to maintain while rotating the sample during RA-SHG collection. For RA-SHG measurements, incorporating a time-resolved component in addition to sample rotation drastically increases the difficulty of the measurements as well as the noise level of the data. Through the interpretation of transient RA-SHG responses, the connection of an analytical bond-based model to the phenomenological sample rotational azimuthal model ultimately fails to provide a reliable picture of transient interatomic potentials, dipole populations, and fields.

Here, I propose a novel phenomenological fit *and* an experimental method to encompass all available orientational transient behaviors without the need to rely on a bond-based model or an inherently noisy experimental method. Along the same lines as what has been previously developed for polarization analyses in biological samples, I base this approach on a tensor analysis of the second order nonlinear optical susceptibility tensor elements with respect to the incident optical fields as a function of input polarization angles. This fit includes 23 possible second order nonlinear optical susceptibility tensor elements, which were not accessible in the RA-SHG phenomenological models. From these tensor elements, one can extract general information on the transient interatomic potentials and lattice polarizations after photoexcitation. I develop this model with a three-dimensional (3D) approach adapted for the TR-PRSHG geometry and apply it to the changes in spatiotemporal interatomic potentials and lattice polarization after femtosecond photoexcitation.

The purpose of the present study is to extract contributions to the polarization-dependent ultrafast SH intensities of a noncentrosymmetric surface in terms of $\chi_{ijk}^{(2)}$ tensor elements. This nonlinear optical behavior is characterized by subpicosecond ultrafast dipole behavior, which interpolates across the depletion field. In this work, I investigate an experimental method able to extract information on the pump-induced surface in III-V semiconductors from transient polarized second harmonic generation (TR-PRSHG). The subpicosecond behaviors of this surface are estimated by monitoring SHG intensity as a function of polarization angle and time delay between pump and probe beams. We introduce a three-dimensional spatiotemporal approach allowing the retrieval

of information not available in traditional azimuthal-oriented methods.

5.2 Experimental Methods

The transient PRSHG (TR-PRSHG) setup used in this work is similar to the PRSHG setup has been described in Chapter 4. The excitation light source is a tunable 76 MHz Ti:sapphire laser delivering 120 fs pulses with an average power of 1200 mW. This source is split into a pump beam and a probe beam with a 50/50 beam splitter. A retroreflector mounted to a translation stage on the pump beam line delays the time between pump and probe pulses, allowing control of ultrafast observations. For each value of Δt (the time delay between pump and probe beam pulses) and each value of φ (the probe polarization angle relative to the collision plane), a SHG intensity measurement is recorded for a total of 61 angles between 0° and 360° at 41 time points between -800 fs to 1200 fs.

The 400 nm SHG probe is separated from the 800nm reflected probe by a band-pass filter and directed into a photomultiplier tube. The total intensity is collected with a lock-in amplifier set to the frequency of the pump beam chopper. The linear polarization of the incident probe beam is continuously rotated in the collision plane by a half-wave plate mounted on a step rotation motor before the sample surface. The linear polarization of the pump beam remains horizontally polarized (p-polarized) throughout the measurement. Finally, the PMT voltage and lock-in settings were adjusted to separate nonlinear optical response to the level of dark current from the PMT and noise level of the lock-in amplifier. The SHG relative intensity values used in this study to calculate steady-state field dynamics can be considered valid. All fits in this study were performed in OriginPro 9.0.

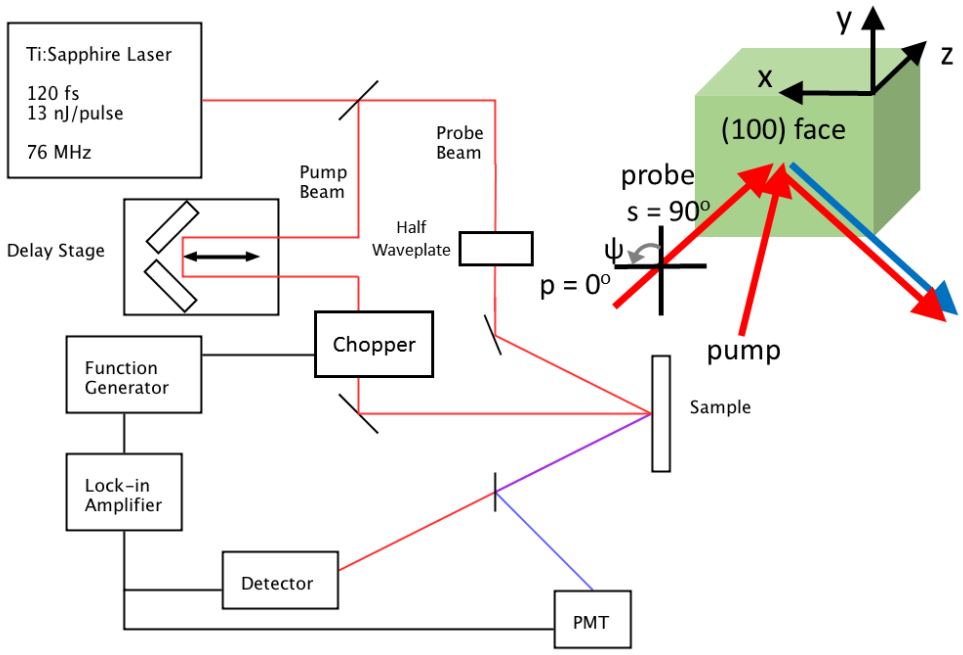

Figure 5.1: Schematic of the setup (a) and sample configuration (b). Probe beam is incident on the sample surface at an incident angle of 45°. Polarization of the probe beam rotates from p-polarization (0° with respect to the collision plane) and s-polarization (90° with respect to the collision plane)

5.3 Model

The second order nonlinear polarization in a Cartesian direction i may be written as a function of the product field amplitudes in the following manner:

$$P_i(\omega_3) = \epsilon_0 \sum_{jk} \chi^{(2)}_{ijk}(\omega_3, \omega_1, \omega_1) E_j(\omega_1) E_k(\omega_1) \tag{31}$$

with

$$d_{ijk} = \frac{1}{2}\chi^{(2)}_{ijk} \tag{32}$$

where $\chi^{(2)}_{ijk}$ is the second-order susceptibility tensor and ijk are Cartesian field components.

Since the focus of this study is on crystalline materials, symmetry conditions and Kleinman contracted notation (d_{ijk}) can further simplify the above expression. Additionally, the SHG response further simplifies the tensor since the input fields in the j and k directions are of the same wavelength ω_1, making the two indices interchangeable. Thus, through this Kleinman symmetry condition simplifies j and k can be into a combined l direction

shown in the table below, where 1, 2, and 3 are x, y, and z, respectively.

Moving to the experimental configuration used in this study, the electric field components E_x, E_y, and E_z for a laser with an incident angle θ I use

$$E(\psi) = \begin{pmatrix} E_x \\ E_y \\ E_z \end{pmatrix} = \begin{pmatrix} E\cos\theta\cos\psi \\ E\sin\psi \\ E\sin\theta\cos\psi \end{pmatrix} \tag{33}$$

where E is the amplitude of the electric field and ψ is the laser polarization with the convention that 0° is p-polarized and 90° is s-polarized. Since the intensity of an electromagnetic field is the square of the electric field and considering an incident angle θ of 45°, the intensity can be described as

$$I(2\omega)_{\psi\to p} = |E_{\psi\to p}(2\omega)|^2 = \left|B_p\cos^2\psi + C_p\cos\psi\sin\psi + D_p\sin^2\psi\right|^2 \tag{34}$$

where

$$\begin{gathered} B_p = \frac{1}{2}(d_{11} + d_{13} + d_{31} + d_{33}) + d_{15} + d_{35} \\ C_p = \sqrt{2}\,(d_{14} + d_{16} + d_{34} + d_{36}) \\ D_p = d_{12} + d_{32} \end{gathered} \tag{35}$$

To allow for fit tolerances, the above expression was expanded which increased the number of fit coefficients to five yielding

$$\begin{aligned} I(2\omega)_{\psi\to p} = {} & H\cos^4\psi + J\cos^3\psi\sin\psi + K\cos^2\psi\sin^2\psi + L\cos\psi\sin^3\psi \\ & + M\sin^4\psi \end{aligned} \tag{36}$$

where

$$\begin{gathered} H_p = B_p^2 \\ J_p = 2B_pC_p \\ K_p = 2B_p\,D_p + C_p^2 \\ L_p = 2C_pD_p \\ M_p = D_p^2 \end{gathered} \tag{37}$$

In the case for the p-out TR-PRSHG responses, these coefficients can be obtained from Eq. (4.27), which can yield nonphysical complex values. To avoid this, I limit the arguments

H and M to be greater than or equal to zero. With this limit, the values for B, C, D, and subsequently the $X_{ijk}^{(2)}$ tensor elements are physical. The tensor element contributions can then be extracted from the p-out and s-out PRSHG data with Eqs. (4.14), (4.22), and (4.27) to produce the relationships in Table 4.2 below.

$X_{ijk}^{(2)}$ **Calculated from Fit Coefficients**	
$\frac{1}{2}(X_{xxx}^{(2)} + X_{zxz}^{(2)} + X_{zxx}^{(2)} + X_{zzz}^{(2)}) + X_{xxz}^{(2)} + X_{zxz}^{(2)}$	$2B_p$
$X_{xyy}^{(2)} + X_{zyy}^{(2)}$	$2D_p$

Table 5.1: Second order transient nonlinear optical susceptibility tensor elements calculated from fit coefficients

5.4 Results and Discussion

TR-PRSHG as a function of time

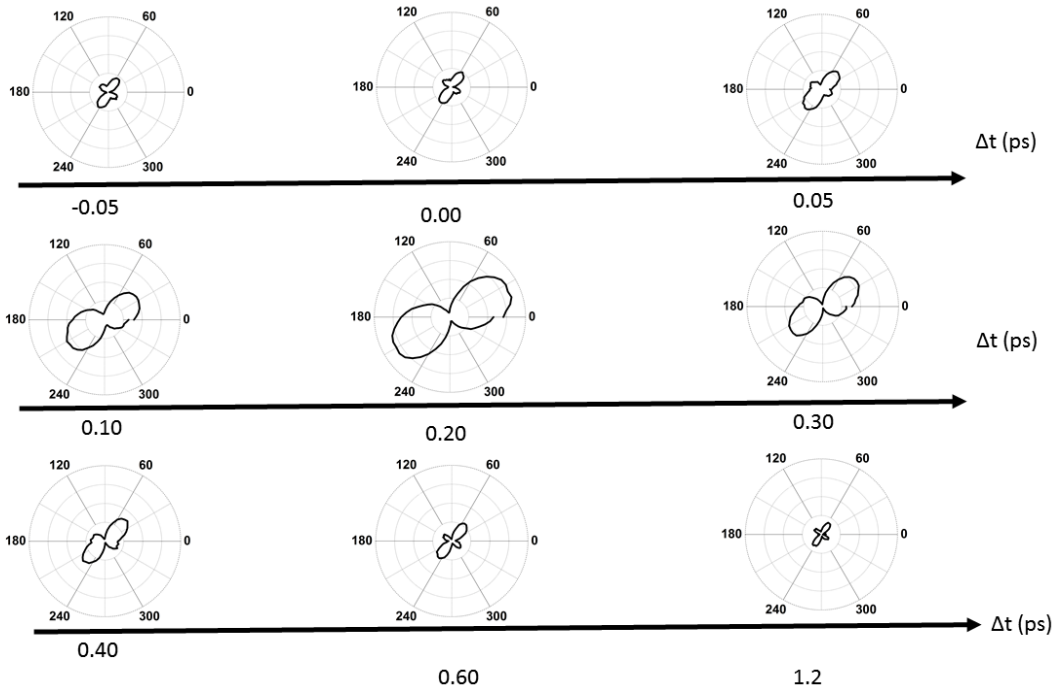

Figure 5.2: (a)Progression of TR-PRSHG data from -800 fs to 1.20 ps for native-oxide GaAs. The peak at 200 fs is highlighted (red line). (b) Progression of select TR-PRSHG data. (c)

Figure 5.2 displays the smooth progression of the TR-PRSHG response for 8 time points between -800 fs and 1200 fs as a function of input polarization angle. Around 50 fs after pump and probe pulse coincidence, the TR-PRSHG response begins to increase until

a peak is achieved at 200fs. Afterwards, the signal begins to decrease towards equilibrium. The progression at this timescale suggests that different subpicosecond processes contribute to transient changes in interatomic potential, which in turn affects the symmetries and amplitudes of the TR-PRSHG response after photoexcitation.

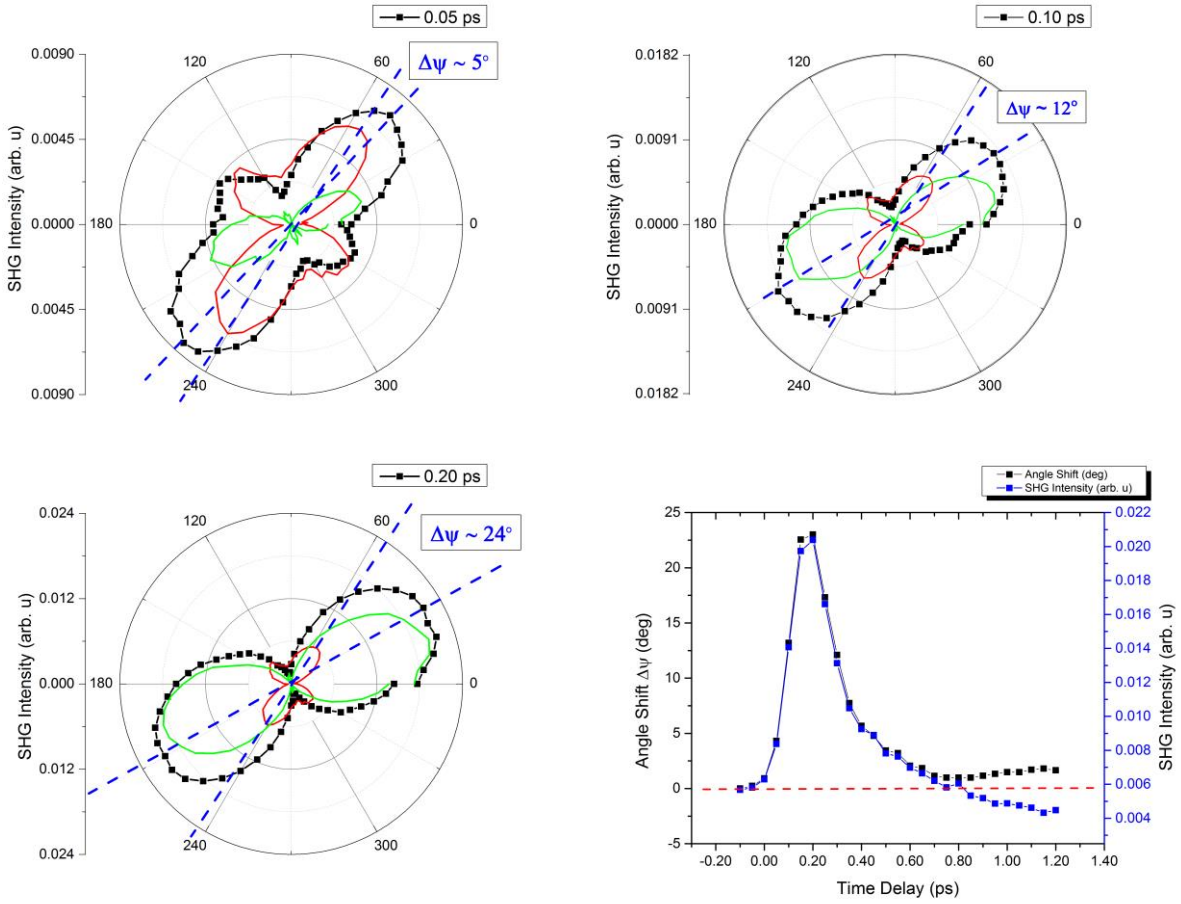

Figure 5.3: TR-PRSHG data of -0.05 ps (a), 0.1 ps (b) and 0.2 ps (c) along with thermal contribution (red lines) and electronic screening contribution (green lines). (d) Angle shift and SHG intensity of the major peak observed in TR-PRSHG data

Within the framework of nonthermal material changes, the total SH response can be written as a unique combination of separate thermal and electronic lattice polarizations. The basis for this assumption is the fact that the lattice does not heat and the atoms do not move from their equilibrium positions until acoustic phonon propagation starts at 4 ps[76,77]. Therefore, the system remains 'nonthermal'. By making the simplification that this thermal equilibrium SH response is constant, observed subpicosecond SH intensity within the first picosecond can be reasonably approximated by the linear superposition of the thermal

equilibrium response and the ultrafast electronic response while the lattice is still cold. These ideas have been developed in linear optical characterization for nonthermal melting phenomena[77-79].

The thermal background transient PRSHG curve has noticeable local maxima at probe polarizations of 54°, 135°, 240°, 325°. Conversely, the photoexcited electronic transient PRSHG curve has local maxima at 24° and 206°. This difference in polarization behavior implies that the driving force of the pump excitation has a different spectral "fingerprint" than background pump-induced changes in interatomic potentials already on the GaAs (100) surface. The cross-section of data in Figure 5.3 shows an overlay of probe input polarizations that are thermally sensitive and which polarizations are electronically sensitive during photoexcitation. The combination of these 2 contributions create an apparent shift of about 22° observed in the major peak in the TR-PRSHG data shown in Figure 5.3d. This illustrates the angle shift and peak TR-PRSHG intensities as a function of time with blue and black markers, respectively. The largest shift is observed around 200 fs after pump excitation. A maximum at 200 fs in both angle shift and TR-PRSHG intensity are observed, 22.5° and 0.021, respectively. Afterwards, they decay similarly until around 800 fs.

At early time delays, the electronic contribution is smaller than or equal to the thermal contribution until pump and probe pulse coincidence at 0 ps. Around 50 fs after coincidence, the TR-PRSHG amplitudes begin to increase until a peak is achieved at 200fs. The difference between the thermal background PRSHG (red) observed -0.8 ps pre-coincidence and the PRSHG at 50 fs yielded what could be considered the photoexcited electronic contribution (green) to the transient PRSHG signal. At 200 fs, this difference in polarization behavior implies that the driving force of the excitation has a *larger* influence on the TR-PRSHG spectrum than the background pump-induced interatomic potential already on the GaAs (100) surface. Around 200 fs in Figure 5.3, the thermal contribution is dwarfed by the electronic contribution. Afterwards, the trend reverses and the signal begins to decrease towards equilibrium behavior for the rest of the experimental time window.

The subpicosecond changes in the TR-PRSHG spectra can be directly related to well-known excitation scattering events covered in depth in Chapter 2. These events and timescales for GaAs are discussed here in some detail. In the first 10 fs, the excited electrons and holes are considered coherent, meaning that they are still polarized along excitation optical field. In the

first 50 fs, the carriers are depolarized through optical phonons but still have not reached a common temperature. That doesn't happen until around 200 fs. At that time, carriers lose energy with each other through carrier-carrier scattering until they reach an effective electronic temperature. Once they reach a common temperature around 4 ps, the carriers cool to the now-increasing lattice temperature (which has remained cool until this point) with the energy transfer through acoustic phonons. After 4 ps, the now-hot lattice and electrons cool to equilibrium together with acoustic phonon decay. The electrons and holes then recombine within 100 ps after photoexcitation. The lattice then continues to cool until the next pump pulse 13 ns later[80].

With this information, it is straightforward to designate the physical origins of the interatomic potential changes that affected the observed TR-PRSHG data. Based on known scattering processes, suggestions can be made. The following processes can be distinguished in the shift shown in Figure 5.2c:

- 0-200 fs: The increase of the angle shift and max TR-PRSHG happens at the same time as carrier thermalization. The largest change in lattice polarization happens here.
- 200 fs – 1200 fs: The pump-induced changes in interatomic potentials and lattice polarization decrease during optical phonon generation. Carriers lose energy through the generation of optical phonons, but the lattice is still cold.
- -800 fs (13 ns after the previous pump pulse) - 0 fs: The lattice has reached an equilibrium temperature and the pump-induced interatomic potential and lattice polarization has returned to equilibrium levels.

Another important feature to note in Figure 5.2c is that the angle shift and peak TR-PRSHG intensities appear to deviate around 800 fs. The angle shift starts to increase while the TR-PRSHG intensity continues to decrease. The red dashed line is the average pre-coincidence value for both the angle shift and max TR-PRSHG intensities. Here, neither the angle shift nor the max SHG intensity returns to equilibrium levels with the greatest variation around 1.2 ps. This deviation suggests that the max peak shift returns to equilibrium while the TR-PRSHG intensity continues to decrease. The comparison of the PRSHG at two times are shown in Figure 5.4 below.

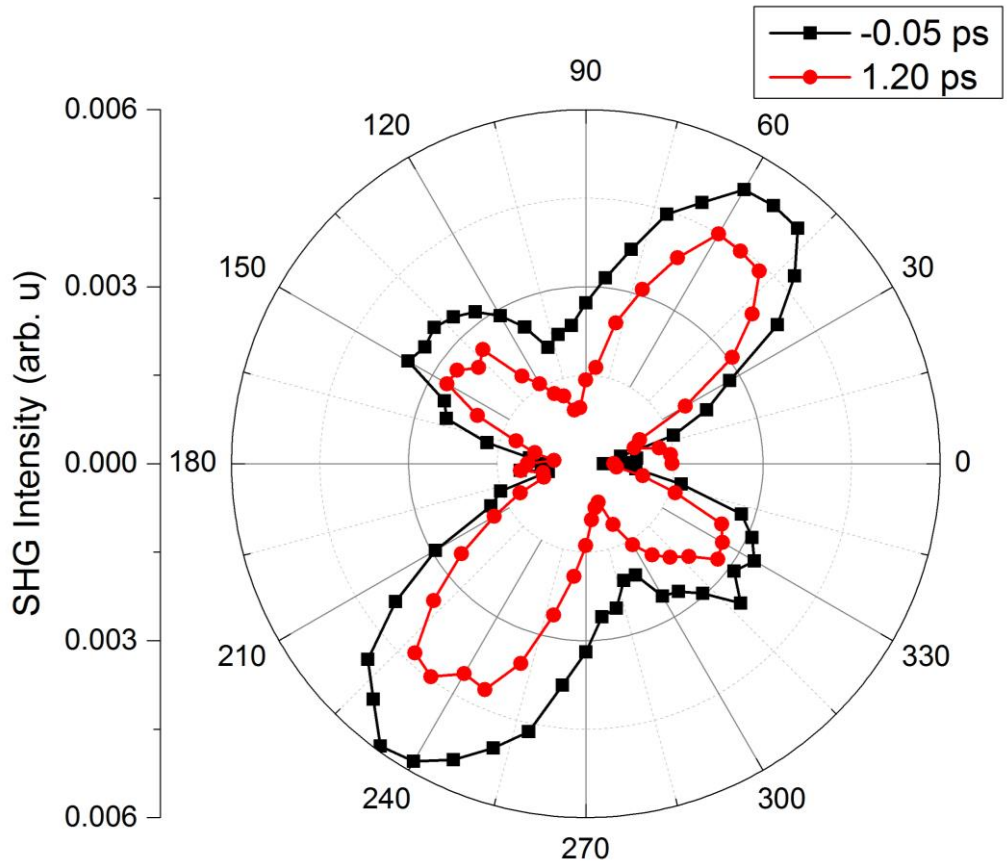

Figure 5.4: TR-PRSHG data of -0.05 ps (black squares) precoincidence and 1.20 ps (red circles) renormalization.

Figure 5.4 presents the TR-PRSHG data in the thermal precoincidence regime (-0.05 ps) as well as the renormalization (1.2 fs) regime. A preliminary analysis of the data has revealed several very interesting observations. Although the symmetries (relative local maxima and minima) remain the same, a difference in absolute amplitudes between the two is observed. A lattice polarization recovery can explain this dramatic return to its initial directional symmetry; however, the lattice polarization at 1.2 ps does not have the same amplitude as the precoincidence thermal regime. To understand which directions of the lattice polarization are sensitive to this phenomenon, one must extract the $X_{ijk}^{(2)}$ tensor elements.

Extraction of $X_{ijk}^{(2)}$ tensor elements from TR-PRSHG data

As the TR-PRSHG spectra, and to a lesser extent the lattice polarization contributions, vary widely as a function of time, it is necessary to extract the major tensor elements to understand pump-induced lattice deformations to the interatomic potentials.

Fortunately, the fit derived in Chapter 4 and reviewed in Section 5.2 enable the extraction of these tensor elements. This section provides the tensor elements required to describe the dynamic response analysis of the lattice after excitation.

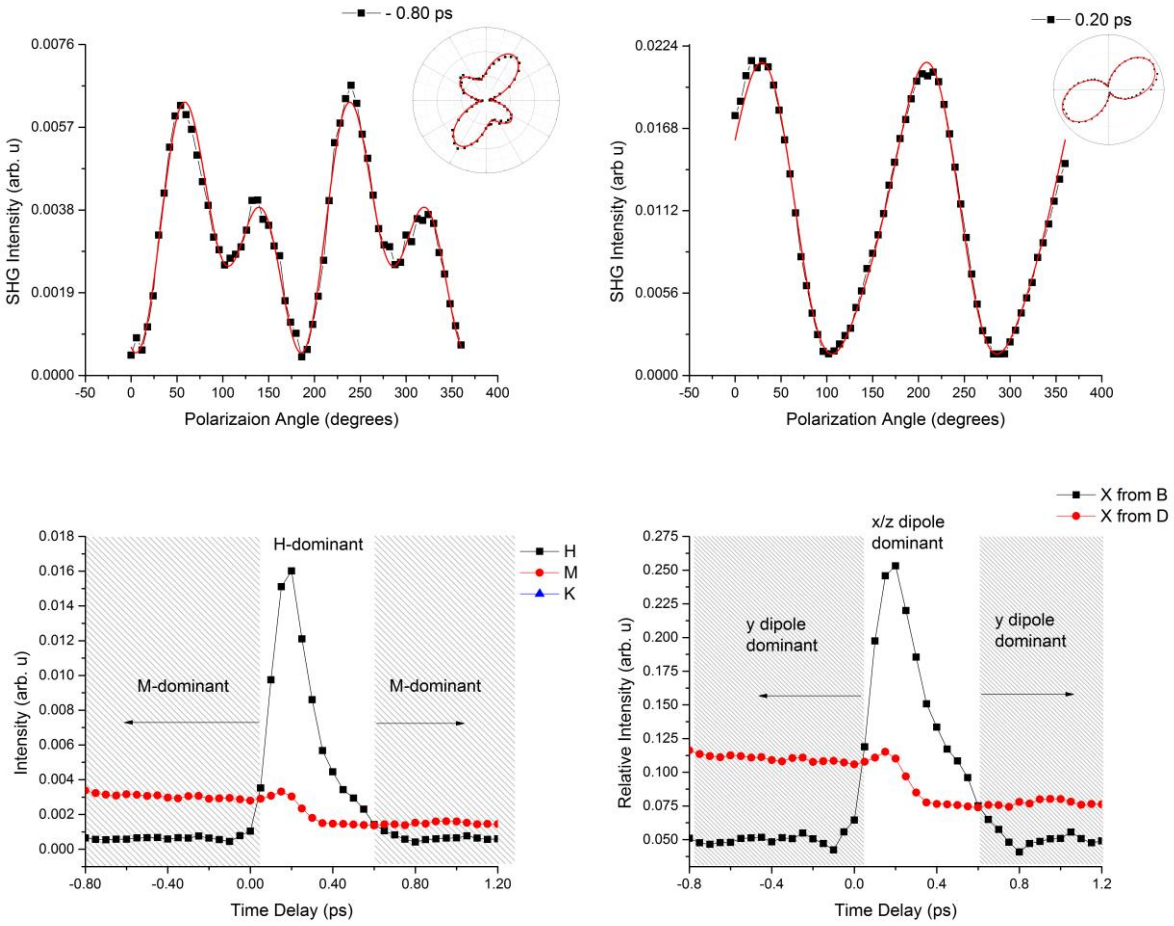

Figure 5.5. TR-PRSHG of native-oxide GaAs (100) -800 fs(a) before coincidence and 200 fs (b) after coincidence with fits. (c) The fit coefficients H (black squares) and M (red circles) as a function of time delay from TR-PRSHG data. (d) The tensor elements from Table 5.1. The lines serve as guides to the eye for their respective curves.

Figure 5.5a and 5b show the input probe polarization dependence of the TR-PRSHG p-out intensity at -800 fs (thermal regime) and 200 fs, respectively. The black markers in both graphs are the TR-PRSHG data collected at each polarization angle (φ). At negative time delays, the curves have typical behavior of stable ultrafast optical responses of semiconductors. The steady level responses of the coefficients reflect the unchanging pump-induced thermal equilibrium. The red lines are the fits from Equations 4.16 for TR-PRSHG intensities as a function of incident probe polarization angle. Due to the closeness of fit for both cases,

the fit coefficients and second order tensor elements can be considered valid. With this fit, the local maxima and minima are of similar amplitudes at their respective input polarization angles for both cases.

In the following discussion, emphasis is placed on the temporal variation in fit coefficients, second order nonlinear susceptibility tensor element groups, and induced lattice polarization after ultrafast excitation. Figure 5.5c shows the time dependence of the H and M coefficients from Equation 4.26. For the other two coefficients, there are three major regimes which have different responses. The basic nonlinear response can be split into three characteristic time periods considered below:

- M dominant before 50 fs
- H dominant between 50 and 500 fs
- M dominant after 500 fs

Within statistical fluctuations, both the $\frac{1}{2}(X_{xxx}^{(2)} + X_{zxz}^{(2)} + X_{zxx}^{(2)} + X_{zzz}^{(2)}) + X_{xxz}^{(2)} + X_{zxz}^{(2)}$ and the $X_{xyy}^{(2)} + X_{zyy}^{(2)}$ tensor element groups show significant dependence on the time delay after excitation. As has been stressed previously, the tensor elements can be calculated from the fit coefficients H and M. From these, one can relate the change in intensity dominance to three characteristic tensor element dominance regimes as shown in Figure 5.5d.

- Y-dipole $X_{xyy}^{(2)} + X_{zyy}^{(2)}$ dominance before 50 fs
- X-dipole $\frac{1}{2}(X_{xxx}^{(2)} + X_{zxz}^{(2)} + X_{zxx}^{(2)} + X_{zzz}^{(2)}) + X_{xxz}^{(2)} + X_{zxz}^{(2)}$ dominance between 50 and 500 fs
- Y-dipole $X_{xyy}^{(2)} + X_{zyy}^{(2)}$ dominance returns after 500 fs

According to the quantum-mechanical formalism of the second order nonlinear optical susceptibility tensor discussed in Chapter 2, the last two indices of a tensor element are defined as the directions of the dipole transition populations contributing to SHG. From Figure 5.5d, the dominant dipole populations transition change from the y-based $X_{xyy}^{(2)} + X_{zyy}^{(2)}$ to the x and z-based $\frac{1}{2}(X_{xxx}^{(2)} + X_{zxz}^{(2)} + X_{zxx}^{(2)} + X_{zzz}^{(2)}) + X_{xxz}^{(2)} + X_{zxz}^{(2)}$ and back again. Clearly, the dominant dipole transition populations are connected to the transport of surface lattice polarization in the depletion region after photoexcitation as well as transient changes in the surface interatomic potentials. Specifically, this can be interpreted as an indication that transient screening of the depletion field

affects dipole populations and interatomic anharmonic potentials smoothly but inhomogeneously.

As can be seen, the x/z tensor element group exhibits a smooth return to equilibrium within the first picosecond. In addition, two drastically different decay behaviors can be observed. The x/z dipole populations rise until a peak at 200 fs and then decay smoothly back to near equilibrium. The y dipole populations have a small bump after excitation around 200 fs followed by a sharp drop which persists beyond 1.2 ps. While it fully recovers by 13 ns, the y dipole population recovery would need to be directly observed with a longer time window than 1.2 ps.

By separating the y from the x/z tensor components, one can extract the decay lifetimes of these ultrafast dipole populations and the ultrafast changes in interatomic potentials. In Figure 5.5d, the y dipole populations are longer lived than the x/z dipole populations. However, to compare the subpicosecond behavior of the y and x/z dipoles, each was fitted to a single-exponential decay equation. Within the first picosecond after excitation, the y dipoles have a lifetime of $\tau_{y1} = 0.06882$ ps^{-1} and the x/z dipoles have a lifetime of $\tau_{xz} = 0.23114$ ps^{-1}.

In this way, I have demonstrated that one can correlate subpicosecond nonlinear behaviors to ultrafast material behaviors in polar semiconductors with TR-PRSHG data and a polarization-resolved fit. This has not been demonstrated with traditional transient SHG experiments with their phenomenological fits. In previous studies, change in ultrafast second harmonic intensities were mostly attributed to a change in a single $\chi_{ijk}^{(2)}$ element[25]. However, that is not reflected in this study.

5.5 Conclusions

In this chapter, I have introduced a phenomenological approach for the analysis of transient polarization-dependent SHG (TR-PRSHG) microscopy measurements applied to the GaAs (100) surface. This approach is based on a 3D tensor analysis of polarization-resolved second harmonic generated intensities to the second order nonlinear optical susceptibility tensor elements as a function of time. The obtained tensor element relationships are shown to contain richer information than either previous models. With a polarization-resolved and time-resolved measurement and fit, it is possible to illustrate 3D dynamics of interatomic potentials and dipole transition populations of III-V semiconductors upon photoexcitation.

Chapter 6

Dissertation Summary and Future Work

This chapter summarizes the dissertation, discusses findings, reviews limitations of the current work, and outlines opportunities for future work. The application of an analytical fit on static and transient PRSHG dependencies has been demonstrated to be a means of understanding macroscopic interatomic potentials and bond polarizations in III-V semiconductors. However, extensions of this research into other semiconductors and crystalline materials deserve further consideration.

This chapter is divided into five sections. Section 6.1 is a summary of the dissertation. Section 6.2 reviews the motivations and objectives of the work done in this dissertation. Section 6.3 summarizes the major discussions. Section 6.4 reviews the limitations of the fits derived in this work. Finally, Section 6.5 brings the dissertation to a close with a review of possible future research directions.

6.1 Summary of Dissertation

This dissertation was organized as follows. Chapter 2 presented a background to the fields of semiconductor physics, electronic band structures, and the origin of nonlinear optics from the perspectives of both classical and quantum mechanics. It thus provided a framework for describing the static and transient nonlinear optical behaviors observed in this work. These topics are related in that they involve linear and nonlinear subpicosecond optical responses in III-V semiconductors undergoing excitation above the band gap.

Next, Chapter 3 motivated the experimental and analytical methods for the studies outlined in Chapters 4 and 5. Chapters 4 and 5 dealt with the experimental and theoretical studies of this dissertation project. Chapter 4 was devoted to the study of polarization-resolved second-order nonlinear optical responses of various III-V semiconductor architectures resulting from strain, defect-conducive growth conditions, and substrate choices. Simplified phenomenological fits for the polarization-dependent second harmonic generation (PRSHG) were first derived with tensor analysis, and then these were fit to the experimental data. The formalism was tested under different conditions to gauge the fit robustness and sensitivity for both mechanical and electronic

changes in III-V semiconductors. Along that same vein, Chapter 5 extended this analytical fit to describe ultrafast PRSHG responses of GaAs (100) as a function of transient lateral and normal interatomic potential behaviors within the first picosecond after photoexcitation.

6.2 Objectives of Dissertation Work

The goal of the work done in Chapter 4 (Study 1) was to assess static surface fields, interatomic potentials, and dipole populations in semiconductors undergoing various distortions. One key piece of this assessment is the relationship between distorted surface fields and static nonlinear optical responses. In previous studies, this relationship had been interpreted as changes in lattice symmetry through only one bulk $\chi_{xyz}^{(2)}$ tensor component. However, existing experimental and analytical methods do not provide sufficient means of quantifying only one contribution to SHG. Nor do these methods quantify how lattice symmetry and static $\chi_{ijk}^{(2)}$ elements change with respect to various types of static lattice distortions. Study 1 sought to fill this gap in knowledge by isolating the $\chi_{ijk}^{(2)}$ tensor components that contribute to the static SHG response and symmetry resulting from these distortions.

The major hypothesis to be tested was that different types of distortions affect lattice symmetry as well as interatomic potentials on the surface of III-V semiconductors. This hypothesis depended on the extraction of $\chi_{ijk}^{(2)}$ tensor elements from static SHG measurements as a function of input polarization angle. While such extractions had been performed previously in the Tolk group for silicon[18], it had not yet been operationalized in other semiconductors. This study introduced an analytical approach that aimed to isolate lateral and normal interatomic potential contributions to SHG from their respective $\chi_{ijk}^{(2)}$ elements for distorted crystalline materials. This strategy focused on the following three objectives:

1. SHG symmetry response as a function of incident polarization angle. The first objective was to extend the characterization method developed in previous studies of silicon that focused on the observation of polarization-dependent surface symmetry changes as a function of incident polarization angle. This extension included surface contributions of III-V semiconductors.
2. Changes in surface symmetries as a function of distortion type. The second objective was to observe changes in

lattice surface symmetries of experimental PRSHG data through distortions like strain and band bending.
3. Change in lateral and normal interatomic potentials as a function of distortion type. The final objective was to describe these potentials due to strain and band bending.

The goal of Chapter 5 (Study 2) was to assess the changes in interatomic potentials and dipole populations in GaAs during the first picosecond after photoexcitation. One key piece of this assessment is the relationship between ultrafast excitation and changes in the effective second order nonlinear susceptibility ($\chi_{ijk}^{(2)}$)tensor elements as it related to time-resolved, polarization-resolved second harmonic generation (TR-PRSHG). Previous research has not provided sufficient means of quantifying pump-induced changes in SHG due to transient electric fields in several directions simultaneously. Study 2 aimed to fill this gap in knowledge by isolating the $\chi_{ijk}^{(2)}$ tensor components that contribute to the pump-induced electric fields, interatomic potentials, and transient SHG symmetries.

The major hypothesis to be tested was that pump-induced transient electric fields affect variations in transient SHG with respect to input polarization angle. This hypothesis depended on the extraction of $\chi_{ijk}^{(2)}$ tensor elements from transient SHG due to changing incident optical fields as a function of input polarization angle. This extraction of transient SHG based on input polarization had not yet been operationalized in previous research. This study introduced an analytical approach that aimed to isolate transient fields in the x, y, and z directions from their respective $\chi_{ijk}^{(2)}$ elements. This strategy focused on the following three objectives:

1. Pump-induced symmetry change as a function of time. The first objective was to extend the characterization method developed in Study 1 that focused on the observation of polarization-dependent surface symmetry change as a function of time.
2. Change in the interatomic potentials and dipole populations as a function of time. The second objective was to apply the analytical model developed in Study 1 to describe the transient behaviors both lateral and normal to the free surface.
3. Decay of transient fields. The final objective was to characterize the decay of lateral and normal transient

fields and potentials to see if they were anisotropic or isotropic.

6.3 Discussion

In Chapter 4, I implemented polarization-resolved SHG spectroscopy and phenomenological fits to probe the orientation of the surface interatomic potentials on high-defect low-temperature grown III-V heterostructures as well as bare III-V semiconductors. In principle, one should be able to use the polarization-resolved nonlinear optical responses to characterize surface defects caused by growth and structural conditions of semiconductors. Specifically, I have applied a polarization-resolved model to study the surface lattice polarizations of free and buried interfaces of III-V semiconductors in three cases. The phenomenological fit developed in Chapter 4 has been shown to qualitatively reproduce most of the experimental features of the PRSHG spectra from free interfaces, growth-mediated defects, and strained thin films. By fitting this to the data, it was possible to relate SH intensities to specific polarization changes in the depletion region caused by defects, surface strain, and surface band structure from the relationships between all 27 $\chi_{ijk}^{(2)}$ tensor elements.

In Chapter 5, I introduced a phenomenological fit for the analysis transient polarization-dependent SHG (TR-PRSHG) measurements applied to the GaAs (100) surface. This approach is based on a 3D derivation of polarization-resolved second harmonic generated intensities to the second order nonlinear optical susceptibility tensor elements. This angular decomposition of the SHG polarization responses showed an anisotropic dependence as a function of time. The obtained tensor element relationships were shown to contain richer information than previous models. With a polarization-resolved, time-resolved measurement and fitting approach, it is possible to illustrate 3D dynamics of interatomic potentials and dipole transition populations of semiconductors upon photoexcitation.

In this way, I demonstrated that one can correlate subpicosecond nonlinear responses to ultrafast behavior in polar semiconductors with TR-PRSHG data and a polarization-resolved fit. This had not been demonstrated with traditional transient SHG experiments or phenomenological fits. In previous studies, changes in ultrafast second harmonic intensities were mostly attributed to

a change in a single $\chi_{ijk}^{(2)}$ tensor element. However, that is not reflected in this data or fit.

6.4 Limitations

A crucial limitation of the polarization-resolved analytical model of SHG is that it only considers interatomic potentials and dipole populations caused by structural changes while ignoring electronic resonances. Specifically, the model does not account for resonant s-output PRSHG from the GaSb/AlGaAs system as shown in Chapter 4. This suggests that the resonant electronic contributions to the PRSHG spectra may not be as easily modeled with this method. The sensitivity shown by this fit is such that one can refine PRSHG response by varying experimental parameters such as wavelength to induce resonant PRSHG responses. To understand this further, the GaAs/AlGaAs sample should be studied at various wavelengths away from the band gap of AlGaAs.

Another limitation of this model is the inability to determine which specific bond movements contribute to the PRSHG or TR-PRSHG intensities. Currently, the fit used in this dissertation perceives SHG as a function of 3 Cartesian directions with respect to the sample surface. However, this perception does not translate well to a microscopic bond picture. Specifically, the microscopic theoretical bond charge model condenses all material behavior to four tetragonal bonds. For strained III-V semiconductors used in this dissertation, only four bonds could not reproduce the misfits and dislocations. Consequently, I could not make determinations on movements of charges along specific deformed bonds that would contribute to PRSHG and TR-PRSHG measurements through the analytical fit developed in this dissertation.

6.5 Future Work

Although the fit developed in this dissertation is not accurate for determining which tensor elements contribute to resonant PRSHG intensities, it does provide an appropriate starting point for more detailed models of the PRSHG spectra. More importantly, the primary advantage of this approach is its applicability to both surface and bulk polarizations. In conclusion, such work leads the way to structural quantitative characterization of all types of crystalline materials. In this section, I review several opportunities for extending the direction and scope of this research.

The first extension of this work is to explore the parameter space for the experiments performed in this dissertation. For instance, one could vary wavelength to observe changes in the static and transient interatomic potentials. By changing the incident wavelengths, it is possible to engage different energy levels and resonances. Another parameter would be the pump polarization. For all transient experiments performed in this dissertation, the incident pump polarization remained horizontally polarized (0°). The anisotropic decay behavior of the bond dipoles may be sensitive to the incident pump polarization. In order to test this, the pump polarization can be changed to circular or elliptical polarization.

Another extension of this work is to test and analyze static and transient interatomic potential profiles in silicon and other Group IV semiconductors. Ideally, studying behaviors at excitation energies around the indirect band gaps of these materials could easily identify any resonant bond behaviors. Since the SHG responses from these materials are so weak due to bulk centrosymmetry, a more sensitive detector like a cooled PMT would be required to perform these experiments. The resulting fundamental research from these experiments would directly apply to both photonic and CMOS devices.

Other materials sensitive to the optoelectronic industry lends itself easily studied with these experimental techniques and analysis. Two dimensional materials such as graphene, molybdenum disulfide, and dichalcogenides would have great surface sensitivities with any given substrate which could then be characterized with polarization-resolved nonlinear optical techniques.

6.6. Conclusions

This dissertation lays the foundation for a new approach to surface interatomic potential characterization of interfaces. Analysis of nonlinear optical responses enable the understanding of interfaces. This approach is not intended to be used as a substitute for diffraction-based structural characterization methods. Nonetheless, it would be a useful complement to existing transient and static structural characterization techniques.

REFERENCES

1. King, R. R. *et al.* 40% efficient metamorphic multijunction solar cells Limiting efficiencies of ideal single and multiple energy gap terrestrial solar cells 40% efficient metamorphic GaInP/ GaInAs/ Ge multijunction solar cells. *Cit. Appl. Phys. Lett. Appl. Phys. Lett. Appl. Phys. Lett* **901,** (2007).
2. Bertness, K. A. *et al.* 29.5%-efficient GaInP/GaAs tandem solar cells. *Cit. Appl. Phys. Lett. Appl. Phys. Lett. Appl. Phys. Lett. Phys. Lett. Detail. Balanc. Limit Effic. p-n Junction Sol. Cells Appl. Phys. Lett* **65,** (1994).
3. Khaselev, O. & Turner, J. A. A Monolithic Photovoltaic-Photoelectrochemical Device for Hydrogen Production via Water Splitting.
4. Deutsch, T. *et al.* III-V semiconductor systems for high-efficiency solar water splitting applications. (2013).
5. Smith, A. M. & Nie, S. Semiconductor Nanocrystals: Structure, Properties, and Band Gap Engineering. *Acc. Chem. Res.* **43,** 190–200 (2010).
6. Liarokapis, E., Papadimitriou, D., Rumberg, J. & Richter, W. Raman and RAS Measurements on Uniaxially Strained Thin Semiconductor Layers. *Phys. Status Solidi* **211,** 309–316 (1999).
7. Ruan, C. Y., Vigliotti, F., Lobastov, V. A., Chen, S. Y. & Zewail, A. H. Ultrafast electron crystallography: Transient structures of molecules, surfaces, and phase transitions. *Proc. Natl. Acad. Sci. U. S. A.* **101,** 1123–1128 (2004).
8. Chen, C., Lue, J. & Wu, C. A study of surface and interlayer structures of epitaxially grown group-III nitride compound films on Si (111) substrates by second-harmonic generation. *J. Phys. …* **15,** 6537–6548 (2003).
9. Hohlfeld, J. *et al.* Electron and lattice dynamics following optical excitation of metals. *Chem. Phys.* **251,** 237–258 (2000).
10. Levine, B. F. Electrodynamical Bond-Charge Calculation of Nonlinear Optical Susceptibilities. *Phys. Rev. Lett.* **22,** 787–790 (1969).
11. Levine, B. F. A New Contribution to the Nonlinear Optical Susceptibilityi Arising from Unequal Atomic Radii. *Phys. Rev. Lett.* **25,** 440–443 (1970).
12. Boyd, R. W. *et al.* Nonlinear Optics. *Nonlinear Opt.* **18,** 543–560 (2008).
13. Boyd, R. W. Nonlinear Optics. *Book* 613 (2008). doi:10.1117/1.3115345
14. Sipe, J. E., Moss, D. J. & Van Driel, H. M. Phenomenological

theory of optical second- and third-harmonic generation from cubic centrosymmetric crystals. *Phys. Rev. B* **35**, 1129–1141 (1987).
15. Lüpke, G., Bottomley, D. J. & van Driel, H. M. Second- and third-harmonic generation from cubic centrosymmetric crystals with vicinal faces: phenomenological theory and experiment. *J. Opt. Soc. Am. B* **11**, 33 (1994).
16. Powell, G. D., Wang, J.-F. & Aspnes, D. E. Simplified bond-hyperpolarizability model of second harmonic generation. *Phys. Rev. B* **65**, 205320 (2002).
17. Germer, T. A., Kołasin-acuteski, K. W., Stephenson, J. C. & Richter, L. J. Depletion-electric-field-induced second-harmonic generation near oxidized GaAs(001) surfaces. *Phys. Rev. B* **55**, 10694–10706 (1997).
18. Park, H., Qi, J., Xu, Y., Lüpke, G. & Tolk, N. Polarization-dependent temporal behaviour of second harmonic generation in Si / SiO2 systems. *J. Opt.* **13**, 55202 (2011).
19. Lyubchanskii, I. L. *et al.* Second-harmonic generation from realistic film–substrate interfaces: The effects of strain. *Appl. Phys. Lett.* **76**, 1848 (2000).
20. Jeong, J.-W. *et al.* Direct observation of controlled strain-induced second harmonic generation in a Co[sub 0.25]Pd[sub 0.75] thin film on a Pb(ZrTi)O[sub 3] substrate. *Appl. Phys. Lett.* **90**, 44108 (2007).
21. Sun, Y., Thompson, S. E. & Nishida, T. Physics of strain effects in semiconductors and metal-oxide-semiconductor field-effect transistors. *J. Appl. Phys.* **101**, 104503 (2007).
22. Tahini, H., Chroneos, A., Grimes, R. W., Schwingenschlögl, U. & Dimoulas, A. Strain-induced changes to the electronic structure of germanium. *J. Phys. Condens. Matter* **24**, 195802 (2012).
23. Jeong, J.-W., Shin, S.-C., Lyubchanskii, I. & Varyukhin, V. Strain-induced three-photon effects. *Phys. Rev. B* **62**, 13455–13463 (2000).
24. Schriever, C., Bohley, C., Schilling, J. & Wehrspohn, R. B. Strained Silicon Photonics. *Materials (Basel).* **5**, 889–908 (2012).
25. Hohlfeld, J., Grosenick, D., Conrad, U. & Matthias, E. Femtosecond time-resolved reflection second-harmonic generation on polycrystalline copper. *Appl. Phys. A* **60**, 137–142 (1995).
26. Hohlfeld, J., Conrad, U. & Matthias, E. Does femtosecond time-resolved second-harmonic generation probe electron temperatures at surfaces? **544**, 11 (1997).
27. Nelson, C. A. *et al.* Time-, Energy-, and Phase-Resolved Second-Harmonic Generation at Semiconductor Interfaces. *J. Phys. Chem. C* **118**, 27981–27988 (2014).

28. Chang, Y.-M., Xu, L. & Tom, H. W. K. Coherent phonon spectroscopy of GaAs surfaces using time-resolved second-harmonic generation. *Chem. Phys.* **251**, 283–308 (2000).
29. Wilcox, D. E., Sykes, M. E., Niedringhaus, A., Shtein, M. & Ogilvie, J. P. Heterodyne-detected and ultrafast time-resolved second-harmonic generation for sensitive measurements of charge transfer. *Opt. Lett.* **39**, 4274 (2014).
30. Park, H., Gutierrez, M., Wu, X., Kim, W. & Zhu, X. Y. Optical probe of charge separation at organic/inorganic semiconductor interfaces. *J. Phys. Chem. C* **117**, 10974–10979 (2013).
31. Brasselet, S. Polarization-resolved nonlinear microscopy: application to structural molecular and biological imaging. *Adv. Opt. Photonics* **3**, 205 (2011).
32. Daum, W., Krause, H.-J., Reichel, U. & Ibach, H. Nonlinear optical spectroscopy at silicon interfaces. *Phys. Scr.* **T49B**, 513–518 (1993).
33. Downer, M. C. Optical Second Harmonic Spectroscopy of Silicon Surfaces , Interfaces and Nanocrystals. **1381**, 1371–1381 (2001).
34. Qi, J. Nonlinear Optical Spectroscopy of Gallium Arsenide Interfaces. 211 (1995). at <http://adsabs.harvard.edu/abs/1995PhDT.....5Q>
35. Fiebig, M. *et al.* Second harmonic generation of magnetic-dipole type in the centrosymmetric antiferromagnets NiO and KNiF3. in *Journal of Magnetism and Magnetic Materials* **258–259**, 110–113 (2003).
36. Pavlov, V. V. *et al.* Magnetic-field-induced second-harmonic generation in semiconductor GaAs. *Phys. Rev. Lett.* **94**, 3–6 (2005).
37. Ma, Z., Wu, K., Sa, R., Ding, K. & Li, Q. Strain-induced improvements on linear and nonlinear optical properties of SrB4O7 crystal. *AIP Adv.* **2**, 0–6 (2012).
38. Zhao, J.-H. *et al.* Strain at Native SiO2/Si (111) Interface Characterized by Strain-Scanning Second-Harmonic Generation. *IEEE J. Quantum Electron.* **47**, 55–59 (2011).
39. Murzina, T. V., Maydykovskiy, A. I., Gavrilenko, A. V. & Gavrilenko, V. I. Optical Second Harmonic Generation in Semiconductor Nanostructures. *Phys. Res. Int.* **2012**, 1–11 (2012).
40. Lüpke, G., Bottomley, D. J. & van Driel, H. M. Second- and third-harmonic generation from cubic centrosymmetric crystals with vicinal faces: phenomenological theory and experiment. *J. Opt. Soc. Am. B* **11**, 33 (1994).
41. Germer, T. A., Kołasin-acuteski, K. W., Stephenson, J. C. & Richter, L. J. Depletion-electric-field-induced second-harmonic generation near oxidized GaAs(001) surfaces. *Phys.*

Rev. B **55**, 10694–10706 (1997).
42. Fiebig, M., Pavlov, V. V. & Pisarev, R. V. Second-harmonic generation as a tool for studying electronic and magnetic structures of crystals: review. *J. Opt. Soc. Am. B* **22**, 96 (2005).
43. Reif, J., Rau, C. & Matthias, E. Influence of magnetism on second harmonic generation. *Phys. Rev. Lett.* **71**, 1931–1934 (1993).
44. Fiebig, M., Lottermoser, T., Pavlov, V. V. & Pisarev, R. V. Magnetic second harmonic generation in centrosymmetric CoO, NiO, and KNiF[sub 3]. *J. Appl. Phys.* **93**, 6900 (2003).
45. Fiebig, M. *et al.* Second Harmonic Generation in the Centrosymmetric Antiferromagnet NiO. *Phys. Rev. Lett.* **87**, 137202 (2001).
46. Brevet, P. F. Phenomenological three-layer model for surface second-harmonic generation at the interface between two centrosymmetric media. *J. Chem. Soc. Faraday Trans.* **92**, 4547 (1996).
47. Cundiff, S. T., Knox, W. H., Baumann, F. H., Evans-Lutterodt, K. W. & Green, M. L. Second-harmonic generation at the interface between Si(100) and thin SiO2 layers. *J. Vac. Sci. Technol. a-Vacuum Surfaces Film.* **16**, 1730–1734 (1998).
48. Latour, G., Gusachenko, I., Kowalczuk, L., Lamarre, I. & Schanne-Klein, M.-C. In vivo structural imaging of the cornea by polarization-resolved second harmonic microscopy. *Biomed. Opt. Express* **3**, 1 (2012).
49. Gusachenko, I., Tran, V., Houssen, Y. G., Allain, J.-M. & Schanne-Klein, M.-C. Polarization-Resolved Second-Harmonic Generation in Tendon upon Mechanical Stretching. *Biophys. J.* **102**, 2220–2229 (2012).
50. Gusachenko, I., Latour, G. & Schanne-Klein, M.-C. Polarization-resolved Second Harmonic microscopy in anisotropic thick tissues. *Opt. Express* **18**, 19339 (2010).
51. Yasui, T. *et al.* Observation of dermal collagen fiber in wrinkled skin using polarization-resolved second-harmonic-generation microscopy. *Opt. Express* **17**, 912 (2009).
52. Campagnola, P. Second harmonic generation imaging microscopy: applications to diseases diagnostics. *Anal. Chem.* **83**, 3224–31 (2011).
53. Campagnola, P. J. *et al.* Three-Dimensional High-Resolution Second-Harmonic Generation Imaging of Endogenous Structural Proteins in Biological Tissues. *Biophys. J.* **82**, 493–508 (2002).
54. Malard, L. M., Alencar, T. V., Barboza, A. P. M., Mak, K. F. & de Paula, A. M. Observation of intense second harmonic generation from MoS 2 atomic crystals. *Phys. Rev. B* **87**,

201401 (2013).
55. Brasselet, S. *et al. In Situ* Diagnostics of the Crystalline Nature of Single Organic Nanocrystals by Nonlinear Microscopy. *Phys. Rev. Lett.* **92**, 207401 (2004).
56. Bonacina, L. *et al.* Polar Fe(IO3)3 nanocrystals as local probes for nonlinear microscopy. *Appl. Phys. B* **87**, 399–403 (2007).
57. Heflin, J. R., Figura, C., Marciu, D., Liu, Y. & Claus, R. O. Thickness dependence of second-harmonic generation in thin films fabricated from ionically self-assembled monolayers. *Appl. Phys. Lett.* **74**, 495 (1999).
58. Elshocht, S. Van *et al.* Chiral 1,1′-binaphthyl-based helical polymers as nonlinear optical materials. *Chem. Phys. Lett.* **309**, 315–320 (1999).
59. Véronique Le Floc'h, Sophie Brasselet, *, Jean-François Roch, and & Zyss, J. Monitoring of Orientation in Molecular Ensembles by Polarization Sensitive Nonlinear Microscopy. (2003). doi:10.1021/JP034950T
60. Hsu, W.-T. *et al.* Second Harmonic Generation from Artificially Stacked Transition Metal Dichalcogenide Twisted Bilayers. *ACS Nano* **8**, 2951–2958 (2014).
61. Plocinik, R. M. & Simpson, G. J. Polarization characterization in surface second harmonic generation by nonlinear optical null ellipsometry. *Anal. Chim. Acta* **496**, 133–142 (2003).
62. Miller, J. K. *et al.* Near-bandgap wavelength dependence of long-lived traveling coherent longitudinal acoustic phonons in GaSb-GaAs heterostructures. *Phys. Rev. B - Condens. Matter Mater. Phys.* **74**, 2–5 (2006).
63. Auston, D. H., Johnson, A. M., Smith, P. R. & Bean, J. C. Picosecond optoelectronic detection, sampling, and correlation measurements in amorphous semiconductors. *Appl. Phys. Lett.* **37**, 371 (1980).
64. Zhang, C. *et al.* Defect-enhanced second-harmonic generation in (Si[sub m]Ge[sub n])[sub p] superlattices. *Appl. Phys. Lett.* **72**, 2072 (1998).
65. Liu, X. *et al.* Native point defects in low-temperature-grown GaAs. *Appl. Phys. Lett.* **67**, 279 (1995).
66. Terashima, K., Ohmori, O., Okada, A., Watanabe, M., Nakanisi, T. No Title. *Proc. Semi-Insulating III-V Mater.* 187 (1986).
67. Latour, G., Gusachenko, I., Kowalczuk, L., Lamarre, I. & Schanne-Klein, M.-C. In vivo structural imaging of the cornea by polarization-resolved second harmonic microscopy. *Biomed. Opt. Express* **3**, 1 (2012).
68. Teulon, C., Tidu, A., Portier, F., Mosser, G. & Schanne-Klein, M.-C. Probing the 3D structure of cornea-like

collagen liquid crystals with polarization-resolved SHG microscopy. *Opt. Express* **24,** 16084 (2016).
69. Tokarz, D. *et al.* Ultrastructural features of collagen in thyroid carcinoma tissue observed by polarization second harmonic generation microscopy. *Biomed. Opt. Express* **6,** 3475 (2015).
70. Chmela, P., Petráček, J., Romolini, A., Pascucci, T. & Falciai, R. Comments on directional photoionization model of second-harmonic generation in doped glass fibers. *Opt. Commun.* **113,** 305–314 (1994).
71. Tokarz, D. *et al.* Ultrastructural features of collagen in thyroid carcinoma tissue observed by polarization second harmonic generation microscopy. *Biomed. Opt. Express* **6,** 3475 (2015).
72. Zheng, C. C. *et al.* Ion-implantation induced nano distortion layer and its influence on nonlinear optical properties of ZnO single crystals. *J. Appl. Phys.* **110,** (2011).
73. Alejo-Molina, A., Hardhienata, H. & Hingerl, K. Simplified Bond Hyperpolarizability Model of Second Harmonic Generation, Group Theory and Neumann's Principle.
74. Hardhienata, H. *et al.* Bond Model and Group Theory of Second Harmonic Generation in GaAs(001). 1–18 (2014). at <http://arxiv.org/abs/1408.1185>
75. Glinka, Y. D. *et al.* Ultrafast spin dynamics in GaAs/GaSb/InAs heterostructures probed by second harmonic generation. *Appl. Phys. Lett.* **81,** 220–222 (2002).
76. Prabhu, S. S. & Vengurlekar, A. S. Dynamics of the pump-probe reflectivity spectra in GaAs and GaN. *J. Appl. Phys.* **95,** 7803–7812 (2004).
77. Zijlstra, E. S., Walkenhorst, J. & Garcia, M. E. Anharmonic Noninertial Lattice Dynamics during Ultrafast Nonthermal Melting of InSb. **135701,** 1–4 (2008).
78. Medvedev, N., Tkachenko, V. & Ziaja, B. Modeling of Nonthermal Solid-to-Solid Phase Transition in Diamond Irradiated with Femtosecond x-ray FEL Pulse. *Contrib. to Plasma Phys.* **55,** 12–34 (2015).
79. Siders, C. W. Detection of Nonthermal Melting by Ultrafast X-ray Diffraction. *Science (80-.).* **286,** 1340–1342 (1999).
80. Kuznetsov, A. V. & Stanton, C. J. Theory of coherent phonon oscillations in semiconductors. *Phys. Rev. Lett.* **73,** 3243–3246 (1994).